From ultraluminous X-ray sources to ultraluminous supersoft sources: NGC 55 ULX, the missing link

C. Pinto,[1]★ W. Alston,[1] R. Soria,[2,3] M. J. Middleton,[4] D. J. Walton,[1] A. D. Sutton,[5] A. C. Fabian,[1] H. Earnshaw,[6] R. Urquhart,[2] E. Kara[7] and T. P. Roberts[6]

[1]*Institute of Astronomy, Madingley Road, Cambridge CB3 0HA, UK*
[2]*International Centre for Radio Astronomy Research, Curtin University, GPO Box U1987, Perth, WA 6845, Australia*
[3]*Sydney Institute for Astronomy, School of Physics A28, The University of Sydney, Sydney, NSW 2006, Australia*
[4]*Physics and Astronomy, University of Southampton, Southampton, Hampshire SO17 1BJ, UK*
[5]*Astrophysics Office, NASA Marshall Space Flight Center, ZP12, Huntsville, AL 35812, USA*
[6]*Department of Physics, Centre for Extragalactic Astronomy, Durham University, South Road, Durham DH1 3LE, UK*
[7]*Department of Astronomy, University of Maryland, College Park, MD 20742-2421, USA*

ABSTRACT

In recent work with high-resolution reflection grating spectrometers (RGS) aboard *XMM–Newton*, Pinto et al. have discovered that two bright and archetypal ultraluminous X-ray sources (ULXs) have strong relativistic winds in agreement with theoretical predictions of high accretion rates. It has been proposed that such winds can become optically thick enough to block and reprocess the disc X-ray photons almost entirely, making the source appear as a soft thermal emitter or ultraluminous supersoft X-ray source (ULS). To test this hypothesis, we have studied a ULX where the wind is strong enough to cause significant absorption of the hard X-ray continuum: NGC 55 ULX. The RGS spectrum of NGC 55 ULX shows a wealth of emission and absorption lines blueshifted by significant fractions of the light speed $(0.01–0.20)c$ indicating the presence of a powerful wind. The wind has a complex dynamical structure with the ionization state increasing with the outflow velocity, which may indicate launching from different regions of the accretion disc. The comparison with other ULXs such as NGC 1313 X-1 and NGC 5408 X-1 suggests that NGC 55 ULX is being observed at higher inclination. The wind partly absorbs the source flux above 1 keV, generating a spectral drop similar to that observed in ULSs. The softening of the spectrum at lower ($\sim$ Eddington) luminosities and the detection of a soft lag agree with the scenario of wind clumps crossing the line of sight, partly absorbing and reprocessing the hard X-rays from the innermost region.

Key words: accretion, accretion discs – X-rays: binaries – X-rays: individual: NGC 55 ULX1, XMMU J001528.9-391319.

1 INTRODUCTION

Ultraluminous X-ray sources (ULXs) are bright, point-like, off-nucleus, extragalactic sources with X-ray luminosities above 10^{39} erg s^{-1} that result from accretion on to a compact object. Previous studies have shown evidence of accretion on to neutron stars with strong magnetic fields (e.g. Bachetti et al. 2014; Fuerst et al. 2016; Israel et al. 2016a,b). It is suggested that ULXs are also powered by accretion on to stellar mass black holes ($<100\,\mathrm{M}_{\odot}$) at or in excess of the Eddington limit (e.g. King et al. 2001; Poutanen et al. 2007; Gladstone, Roberts & Done 2009; Liu et al. 2013; Middleton et al. 2013) or accretion at more sedate Eddington ratios on to intermediate mass black holes ($10^{3-5}\,\mathrm{M}_{\odot}$, e.g. Greene & Ho 2007; Farrell et al. 2009; Webb et al. 2012; Mezcua et al. 2016).

Ultraluminous supersoft sources (ULSs) are defined by a thermal spectrum with colour temperature $\sim$0.1 keV, bolometric luminosity $\sim$ a few 10^{39} erg s^{-1}, and almost no emission above 1 keV (Kong & Di Stefano 2003). Deep exposures of ULSs have shown the presence of a hard tail, possibly due to a disc-like emission similar to ULXs (see e.g. Urquhart & Soria 2016). Classical X-ray binaries and ULXs, either have broad-band emission over the 1–10 keV range or a peak disc-blackbody temperature of a few keV. Alternative models have tried to describe the X-ray spectra of ULSs with accreting intermediate-mass and stellar mass black holes like for ULXs or with extreme supersoft sources powered by surface-nuclear-burning on white dwarf accretors (see e.g. Di Stefano & Kong 2004; Feng et al. 2016; Soria & Kong 2016, and references therein).

ULXs and ULSs were initially considered different physical types of systems. However, on the one hand, we have seen strong evidence of winds in classical ULXs (Middleton et al. 2015b;

★ E-mail: cpinto@ast.cam.ac.uk

Pinto, Middleton & Fabian 2016). On the other hand, some ULSs (e.g. in M 101 and NGC 247) exhibit a harder (fast variable) X-ray tail (e.g. Urquhart & Soria 2016), suggesting that some of the X-ray photons occasionally get through a rapidly changing wind (e.g. Middleton et al. 2011; Takeuchi, Ohsuga & Mineshige 2013). It is therefore speculated that ULXs and ULSs are simply two types of super-Eddington accretors, with respectively geometrically thinner and thicker outflows along the line of sight due to different viewing angles or mass accretion rates (e.g. Poutanen et al. 2007; Feng et al. 2016; Urquhart & Soria 2016, and reference therein). To some extent, this scenario is similar to the unification scenario proposed for active galactic nuclei (e.g. Elvis 2000, and references therein). The core of our work is to test this model through the study of a bright and well-isolated transitional object, which looks like a ULX when the wind is not optically thick and then shows some ULS signatures when the wind thickens: NGC 55 ULX.

The study of winds in ULXs and ULSs is now possible after the recent discovery (Pinto et al. 2016, hereafter Paper I) of rest-frame emission and blueshifted absorption lines in NGC 1313 X-1 and NGC 5408 X-1 ULXs, with the high-resolution reflection grating spectrometers (RGS) gratings aboard *XMM–Newton*. Similar features were also found in NGC 6946 X-1, albeit at lower significance. The detections confirm the presence of powerful, relativistic ($\sim 0.2c$), winds in these sources and by extension in several other ULXs with similar spectral residuals (e.g. Stobbart, Roberts & Wilms 2006; Middleton et al. 2015b; Sutton, Roberts & Middleton 2015). The high-ionization Fe K part of the ultrafast outflow in stacked European Photon Imaging Camera and *NuSTAR* spectra of NGC 1313 X-1 was also detected (Walton et al. 2016a).

The timing properties of ULXs provide an independent diagnostic of the accretion process. Heil & Vaughan (2010) first detected a linear correlation between variability amplitude and flux in the ULX NGC 5408 X-1, similar to that found in Galactic X-ray binaries and active galactic nuclei (e.g. Uttley & McHardy 2001; Vaughan et al. 2003). Heil & Vaughan (2010) also found evidence of time delays between soft and hard energy bands, with the softer bands delayed with respect to the hard at frequencies of ~ 20 mHz. These time delays were later confirmed by De Marco et al. (2013) in several newer *XMM–Newton* observations. Delays between spectral components may provide some further clues on the geometry of the system and the different physical emission mechanisms in ULX and ULS accretion discs. They could indeed be related to the different location of the soft/hard X-ray emitting regions.

This paper is structured as follows. In Section 2, we report some well-known characteristics of NGC 55 ULX that motivated us to search for evidence of winds. We present the data in Section 3 and a detailed spectral modelling in Section 4. Covariance and lag spectra of the source are shown in Section 5. We discuss the results and provide some insights on future missions in Section 6 and give our conclusions in Section 7. More technical detail on our analysis is reported in Appendix A.

2 THE ULX–ULS HYBRID IN NGC 55

NGC 55 ULX is the brightest X-ray source in the nearby Magellanic-type galaxy NGC 55 (NASA/IPAC Extragalactic Database average distance 1.94 Mpc[1]) with an X-ray luminosity peak of $\sim 2 \times 10^{39}$ erg s^{-1} (see Table 1 and Fig. 2). The X-ray light curve exhibits a variety of features including sharp drops and 100 s

[1] https://ned.ipac.caltech.edu/

Table 1. *XMM–Newton* observations used in this paper.

ID	Date	t_{pn}^a (ks)	t_{RGS1}^a (ks)	t_{RGS2}^a (ks)	L_X^b
0028740201	2001-11-14	27.2	–	–	2.07
0655050101	2010-05-24	95.3	119.9	119.5	1.30

^{a}EPIC-pn/RGS net exposure time. ^{b}0.3–10 keV luminosity in 10^{39} erg s^{-1} assuming a distance of 1.94 Mpc. No significant RGS data were available during the first (off-axis) observation.
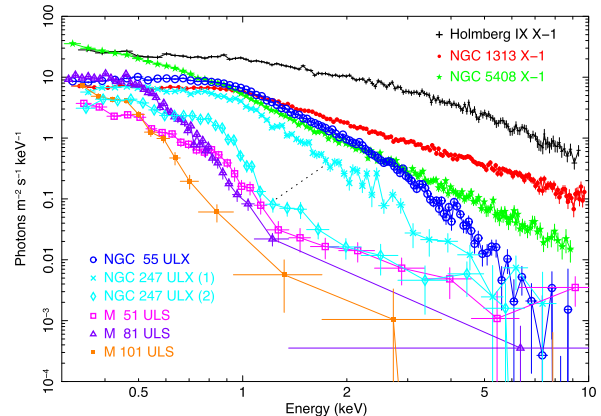
Figure 1. ULX-to-ULS spectral states sequence. A dotted line connects the standard ULS states with the soft ULX states of NGC 247 and NGC 55 ULXs. For more detail see the text.

dips. During the dips most of the source flux is quenched in the 2.0–4.5 keV band. Stobbart, Roberts & Warwick (2004) proposed that the accretion disc is viewed close to edge-on and that, during dips, orbiting clumps of obscuring material enter the line of sight and cause significant blocking or scattering of the hard thermal X-rays emitted from the inner disc.

The EPIC CCD spectra of NGC 55 ULX can be modelled with a broad-band component from the innermost region (either as a disc blackbody or as Comptonization) plus the standard $T \sim 0.15$ keV blackbody, which we see in most ULSs and the softest ULXs and probably originates from reprocessed emission, such as Compton down-scattered emission, and intrinsic disc emission (e.g. Sutton, Roberts & Middleton 2013; Pintore et al. 2015). The spectrum is very soft (slope $\Gamma > 4$, if modelled with a power law) similar to ULSs, but there is significant flux and a bright hard tail above 1 keV (see Section 4.1), which is stronger than typical ULSs (e.g. Urquhart & Soria 2016).

In Fig. 1, we show the observed EPIC-pn spectrum of NGC 55 ULX (*XMM–Newton* observation 0655050101) with a sequence of ULX spectra, from harder to softer: Holmberg IX X-1 (0693851801), NGC 1313 X-1 (0693851201), NGC 5408 X-1 (0653380501), NGC 247 ULX (0728190101 and 0601010101), M 51 ULS (0303420201), M 81 ULS (*Chandra* observation 735) and M 101 ULS (0212480201).

NGC 247 ULX is a very interesting source that oscillate around the boundary between the ULS and the soft ULX regime (see also e.g. Feng et al. 2016). Unfortunately, no deep grating observations are available for this object and for ULSs in general (see Section 6.4). However, the high-flux spectrum of NGC 247 has a similar shape to that of NGC 55 ULX with both sources showing a turnover above 1 keV and, more importantly, is superimposable with the spectrum of the low-flux state of NGC 55 ULX (see e.g. Fig. 9). NGC 55 ULX has never shown a classical ULS spectrum during
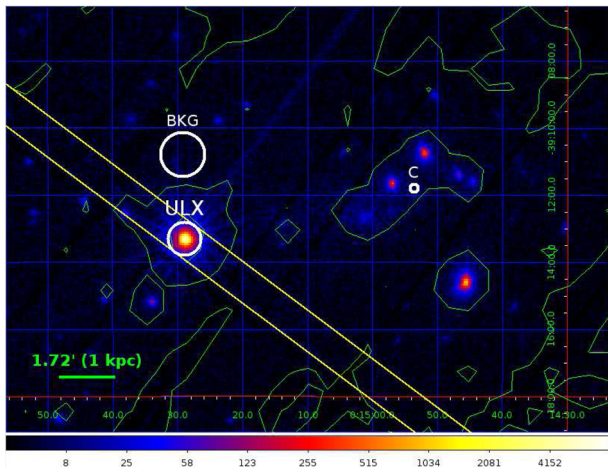
Figure 2. NGC 55 ULX EPIC/pn-mos stacked image. The yellow lines show the extraction region for the RGS spectrum. The bigger larger white circle is the EPIC background region. The smallest circle in the right indicates the NGC 55 galactic centre.

the *XMM–Newton* observations because the fraction of the energy carried by the photons above 1.5 keV has been above 15 per cent, which is higher than the 10 per cent limit commonly used to identify supersoft sources (see e.g. Di Stefano & Kong 2003), but its similarity to NGC 247 ULX, which sometimes looks like a ULS, and its soft spectral shape, which just fits in between the classical ULXs and ULSs, are crucial.

There is a whole on-axis *XMM–Newton* orbit ($\sim$120 ks) of NGC 55 ULX plus other shorter exposures which provide a unique workbench to study the transition between the two phases. The search for a wind in this object is highly motivated by the detection of soft X-ray residuals in the EPIC spectra of NGC 55 ULX that are similar in both shape and energy ($\sim$1 keV) to those that were observed and resolved in other ULXs (see e.g. Middleton et al. 2015b and Paper I).

3 THE DATA

In this work, we utilize data from the broad-band (0.3–10 keV) EPIC-pn CCD spectrometer (Turner et al. 2001) and the high-resolution RGS (0.35–1.77 keV) aboard *XMM–Newton* (den Herder et al. 2001) in order to constrain the spectral shape of the source and to search for evidence of a wind.

The *XMM–Newton* observations used in this paper are reported in Table 1. We decided not to use another available observation (ID = 0028740101) because it had the ULX near the edge of the field of view with a point spread function (PSF) highly distorted and affected by the background. The combination of low flux and short exposure with corresponding limited statistics makes it not useful for our analysis. The exposure with ID 0655050101 is the only one to provide significant RGS science data because the other exposures are off-axis with the ULX outside the RGS ($\pm$2.5 arcmin) field of view.

We reduced the data with the latest *XMM–Newton*/SAS v15.0.0 (CALDB available on2016 September) and corrected for contamination from soft-proton flares. We extracted EPIC MOS 1-2 and pn images in the 0.5–3 keV energy range, which includes the vast majority of NGC 55 ULX photons, and stacked them with the *emosaic* task (see Fig. 2). We also extracted EPIC-pn spectra from within a circular region of 1 arcmin diameter centred on the emission peak.

The background spectra were extracted from within a slightly larger circle in a nearby region on the same chip, but away from bright sources and the readout direction (see Fig. 2). We also make sure that the background region was outside the copper emission ring (Lumb et al. 2002). We also tested three other background regions for the EPIC-pn spectrum to confirm that the background does not produce instrumental features. There was very little solar flaring during the observations.

We extracted the first-order RGS spectra in a cross-dispersion region of 1 arcmin width, centred on the emission peak and the background spectra by selecting photons beyond the 98 per cent of the source PSF and check for consistency with blank field observations. For more detail on the RGS background, see Appendix A1. We stacked the RGS 1 and 2 (for displaying purposes only, using the method described in Paper I). The RGS spectrum of NGC 55 ULX shows very interesting emission-like features and a sharp drop near 11 Å very similar to that one observed in EPIC spectra of ultraluminous supersoft sources (e.g. Urquhart & Soria 2016).

4 SPECTRAL ANALYSIS

4.1 Broad-band epic spectrum

We fitted the EPIC-pn spectrum with the new SPEX code[2] v3.02 to constrain the broad-band continuum. Each of MOS 1 and 2 cameras has three to four times less effective area than pn, which alone contains the vast majority of the counts. The pn spectrum was sampled in channels equal to 1/3 of the spectral resolution for optimal binning and to avoid oversampling. We grouped the pn spectra in bins with at least 25 counts and use χ^2 statistics. Throughout the paper, we adopt 1σ error bars.

We focused on the pn spectrum of the second (0655050101) exposure to determine the best-fitting continuum model because it has twice as many counts as the first observation, shows less variability, and its continuum determination is crucial for following high-resolution analysis. We tested two alternative models to describe the broad-band EPIC-pn spectrum of NGC 55: a combination of blackbody (*bb*) plus power law (*po*) and a combination of blackbody (*bb*) plus disc blackbody modified by coherent Compton scattering (*mbb*, see SPEX manual for more detail). All emission components were corrected by absorption due to the foreground interstellar medium and circumstellar medium (*hot* model in SPEX with low temperature 0.5 eV, see e.g. Pinto et al. 2012).

The double blackbody model (*bb* + *mbb*) provides a better fit than the power-law model (see Table 2) in agreement with the two-component model consisting of a blackbody (for the soft component) and a multicolour accretion disc (for the hard component) of Pintore et al. (2015) for *Chandra* and *Swift* observations of NGC 55 ULX. Moreover, the power-law model would imply a very high luminosity since the deabsorbed model diverges at low energies.

Of course, we cannot exclude one or the other continuum model according to the value of the χ^2 only. A good exercise consists in determining the column density, N_H in a different way or using other observations and compare it to that measured with the blackbody and the power-law models. Pintore et al. (2015) have shown that the N_H of NGC 55 ULX varies over a large range, $1–6 \times 10^{21}$ cm^{-2}, which is always an order of magnitude above the Galactic value ($1–2 \times 10^{20}$ cm^{-2}). Interestingly, if we fit the EPIC data with the power-law model, but excluding the hard tail

---

[2] http://www.sron.nl/spex

Table 2. Constraints on the broad-band continuum model. EPIC-pn $_{(0655050101)}$ spectrum was used for its high-S/N ratio. $L_{X(0.3-10\,keV)}$ luminosities are calculated assuming a distance of 1.94 Mpc and are corrected for absorption (or de-absorbed). Flux percentages are measured between 0.3 and 10 keV.

Parameter	BB + PO	BB + MBB
$L_{X\,po}$ (erg s^{-1})	1.3×10^{40}	–
$L_{X\,bb}$ (erg s^{-1})	1.9×10^{38}	7.4×10^{38}
$L_{X\,mbb}$ (erg s^{-1})	–	5.5×10^{38}
Γ	4.76 ± 0.10	–
kT_{bb} (keV)	0.52 ± 0.09	0.163 ± 0.003
kT_{mbb} (keV)	–	0.69 ± 0.01
N_H (10^{21} cm^{-2})	5.10 ± 0.14	2.07 ± 0.08
χ^2/dof	332/99	191/99

above 2 keV, we obtain 4.1×10^{21} cm^{-2}. If instead we only fit the EPIC spectrum between 0.4 and 1 keV we obtain 2.7×10^{21} cm^{-2}, which may suggest that the broad-band power-law fit overestimates the column density. We have also tested a Comptonization continuum (*comt* model in SPEX with $T_{seed} = 0.13 \pm 0.01$, $T_e = 0.83 \pm 0.03$, and $\tau = 6.8 \pm 0.3$) over the 0.3–10 keV and obtained $2.1 \pm 0.1 \times 10^{21}$ cm^{-2}. Following the procedure of Pinto et al. (2013), adopting solar abundances and a power-law continuum, we have also measured the N_H through the depth of the absorption edges of the most abundant interstellar neutral species in the RGS spectrum: neon (13.4 Å), iron (17.4 Å) and oxygen (23.0 Å), see Fig. 4. We obtained $N_H = 1.5 \pm 0.5 \times 10^{21}$ cm^{-2}, without significant differences whether we fit the whole RGS spectrum or edge-by-edge. This also prefers the solution obtained with the blackbody model.

The harder multicolour component is seen in most ULXs, although its temperature is typically 1.5–2.5 keV (hence the origin of the characteristic downturn at ~ 5–6 keV). In the softest states of ULXs (e.g. in NGC 55 ULX) and in classical ULSs temperature can be as low as 0.7 keV. It is thought to consist of emission produced by the inner accretion disc highly distorted by interaction with hot electrons in the inner regions (up-scattering) and by down-scattering with cool electrons in the wind (e.g. Gladstone et al. 2009; Middleton et al. 2011 a, 2015a). The soft (~ 0.2 keV) component is likely to be intrinsic to regions above the outer disc, where a radiatively driven wind is expected to be launched at accretion rates comparable or higher than the Eddington limit (Poutanen et al. 2007). Our broad-band spectral fits are consistent with NGC 55 ULX being a soft ultraluminous (SUL) X-ray source according to the classification of Sutton et al. (2013).

The first, shorter, observation also favours a multiblackbody emission model. The EPIC spectrum in 2001 basically exhibits hotter blackbody components (see below and Table 5). Interestingly, we found that the emitting area of the soft (~ 0.2 keV) blackbody component increases by a factor 2 from the brighter (2001) to the fainter (2010) observation in agreement with the study of ULSs of Urquhart & Soria (2016) and Feng et al. (2016). This is expected if the expansion of the photosphere and the decrease of the temperature shift the peak of the spectrum from X-ray towards the far-UV.

As previously mentioned, ULSs show a faint hard X-ray tail (>1.5 keV) whose origin is not quite understood. It is thought to be produced in the inner regions similar to ULXs and characterized by either Bremsstrahlung or Comptonization emission (see e.g. Urquhart & Soria 2016). As a test, we have re-fitted the NGC 55 ULX EPIC spectrum by substituting the *mbb* component with a rest-frame Bremsstrahlung or collisionally ionized emission
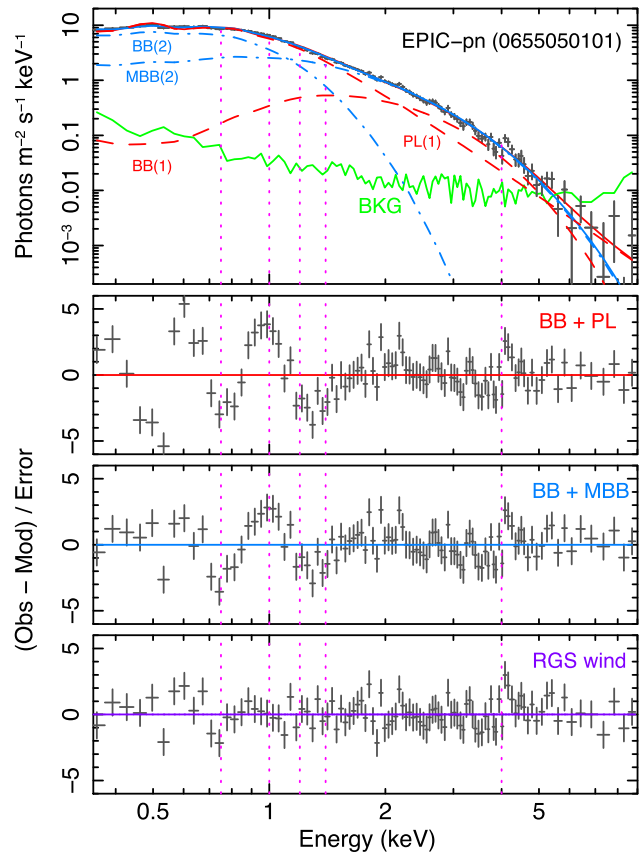
Figure 3. NGC 55 ULX EPIC-pn background-subtracted spectrum with two alternative continuum models (see Table 2). The dotted lines show interesting features that do not depend on the adopted continuum model, some of which can be resolved in the soft X-ray high-resolution RGS spectrum (see Fig. 4). The dotted lines show the model components for Model 1 (BB+PL) and Model 2 (BB+MBB); for more detail see Table 2. The bottom panel shows the EPIC-pn residuals adopting the wind model from the RGS high-resolution spectrum (see Section 4.2.6).
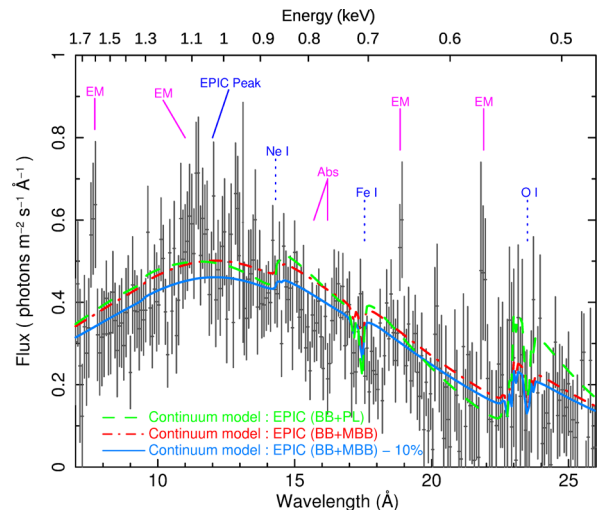
Figure 4. RGS stacked spectrum with the overplotted EPIC best-fitting continuum model (see Table 2). The solid blue line shows the RGS-fitted continuum with free normalization as only free parameter. The wavelengths of expected absorption lines produced by the Galactic absorber (Pinto et al. 2013) and the ~ 1 keV peak seen in the EPIC spectrum are shown by blue dashed lines. Some clear emission- (EM) and absorption-like (Abs) spectral features are marked with solid magenta lines.

model (*cie* model in SPEX). The *bb + brems* fit is bad ($\chi_\nu^2 = 13.8$). We also tried to get an upper limit on the emission of a putative Bremsstrahlung component adding it on the top of the best-fitting *bb + mbb* model. The maximum flux a Bremsstrahlung component can have is 10 times smaller than the flux of the *mbb* component. The Bremsstrahlung temperature was however highly unconstrained. Therefore, if the hard X-ray tail seen in ULSs is similar to the one that is well constrained in NGC 55 ULX, then a disc origin would be favoured.

Although the double blackbody model provides a better fit, it is still statistically rejected. The presence of strong residuals around 1 keV shows an important similarity with the residuals seen in several ULXs with long exposures (emission peak at 1 keV and absorption-like features on both sides). Middleton et al. (2014, 2015b) interpreted them as either due to emission by collisionally ionized gas or to absorption by outflowing photoionized gas and were identified in Paper I. This motivated our investigation with the RGS.

The knowledge of the exact structure of the spectral continuum (either a double blackbody or power law or Comptonization) does not strongly affect the following analysis, which focuses on the search for narrow spectral features and broad-band spectral variations.

4.2 The high-resolution RGS spectrum

4.2.1 RGS spectral continuum

Our analysis focuses on the 7–27 Å first-order RGS 1 and 2 spectra from the long, on-axis, observation 2 (0655050101). Below 7 Å the effective area is not well calibrated and above 27 Å the count rate is too low. For the RGS analysis, we have to use C-statistics because of the Poisson statistics and the need for high spectral resolution. The spectrum was binned in channels equal to 1/3 of the spectral resolution for the optimal binning (see Kaastra & Bleeker 2016).

We plot the EPIC continuum models on top of the RGS data in Fig. 4. As for EPIC, the double blackbody spectral model describes the RGS spectrum better than the blackbody+power law combination, although RGS does not have the same sensitivity. Therefore, the choice of the continuum will not have a significant effect on our results. We fit the EPIC model to the RGS spectrum leaving only the overall normalization as a free parameter and obtained a comparable fit with the overall flux lower by about 10 per cent compared to the EPIC continuum model (see the solid blue line in Fig. 4). This RGS continuum model is used in the following analysis.

One of the major issues in modelling the RGS spectra of faint sources, such as ULXs, is the background. However, NGC 55 ULX is significantly brighter than the background between 7 and 25 Å. Moreover the source is reasonably isolated; the RGS slit does not encounter any other bright object (see Fig. 2) and the background spectrum is rather featureless. For more detail see Appendix A1.

4.2.2 Search for spectral features

Following the approach used in Paper I, we searched for spectral features on top of the spectral continuum by fitting a Gaussian spanning the 7–27 Å wavelength range with increments of 0.05 Å and calculated the Δ C-statistics. We tested a few different line widths: 500, 1000, 5000 and 10 000 km s^{-1}. We show the results obtained with 500 km s^{-1} (∼ RGS resolution) and 10 000 km s^{-1} (a case of relativistic broadening) in Fig. 5. The black points refer to
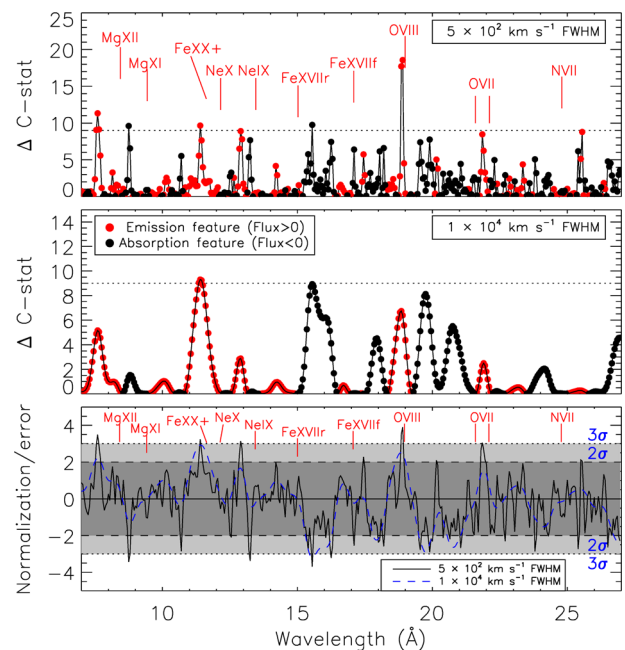
Figure 5. Δ C-statistics obtained by fitting a Gaussian spanning the 7–27 Å wavelength range with increments of 0.05 Å. Δ C = 2.71, 4.00 and 9.00 refer to 1.64σ (90 per cent), 2σ (95.45 per cent) and 3σ (99.73 per cent) confidence levels. We tested the effects of using two different line widths: 500 km s^{-1} (∼ RGS resolution, top panel) and 10 000 km s^{-1} (medium panel). Red and black points refer to emission and absorption lines, respectively. The ratio between the normalization of the Gaussian and its error is shown in the bottom panel. The rest-frame wavelengths of some relevant transitions are labelled. More detail on the line significance is reported in the text.

lines with negative normalizations, i.e. absorption lines. We found several narrow emission features and some evidence for absorption. The emission-like features are near some of the strongest transitions commonly observed in X-ray plasmas and are the same that we have detected in our previous work on NGC 1313 ULX-1, NGC 5408 ULX-1 and NGC 6946 ULX-1. The RGS spectra amplify and resolve the residuals previously detected in the EPIC spectra (Middleton et al. 2015b).

If we identify the emission features with some of the strongest transitions in this energy band – Mg XII (8.42 Å), Fe XXII–XXIII (11.75 Å), Ne X (12.135 Å), Ne IX (13.45 Å), O VIII (18.97 Å) and O VII (21.6 Å, 22.1 Å) – then they would require blueshift, which seems to be larger for higher ionization states. For instance, the spike around 7.5 Å is likely produced by blueshifted Mg XII; the one seen around 11.4 Å could be a blend of blueshifted Ne X and high Fe ions. The 21.8 Å emission-like feature could be a blueshifted O VII 22.1 Å forbidden line. An O VII forbidden line (22.1 Å) stronger than the resonant line (21.6 Å) is a clear indication of photoionization (e.g. Porquet & Dubau 2000). The high-ionization ions, e.g. Mg XII, Fe XXII–XXIII and Ne IX also show strong resonant lines suggesting possible collisional ionization and therefore a complex wind ionization/temperature structure. In the identification process, we assumed that the lines were produced by the strongest transitions in the X-ray band and within ±0.2c from their rest-frame wavelengths. We notice that the blueshifts of the strongest O VII and O VIII emission lines are consistent within 1σ. The same applies to the Mg XII and Ne X emission lines.

In Appendix A7, we show that the features detected in the RGS spectrum of NGC 55 ULX are intrinsic to the sources and are not of

Table 3. NGC 55 ULX XMM/RGS fit : Monte Carlo simulations. Confidence level of the lines detected in the RGS spectrum. The *p*-values were computed with 10 000 Monte Carlo simulations accounting for the number of trials (for more detail see Section 4.2.3). 'E' and 'A' indicate emission and absorption lines, respectively.

λ	7.5 Å	8.75 Å	11.4 Å	15.55 Å	18.9 Å	21.85 Å
Type	E	A	E	A	E	E
p-value	0.005	0.007	0.009	0.009	0.001	0.008
CI	99.5 per cent	99.3 per cent	99.1 per cent	99.1 per cent	99.9 per cent	99.2 per cent
σ	2.8	2.7	2.6	2.6	3.3	2.65

instrumental origin by applying the same line-search technique to the spectra of five active galactic nuclei with comparable statistics.

4.2.3 Monte Carlo simulations

The Δ C-statistics of each feature provides a crude estimate of the significance but does not take into account the look-elsewhere effect, which is due to the size of the parameter space used such as the number of velocity bins used, and other eventual effects due to the data quality. We therefore performed Monte Carlo simulations to estimate the significance of the strongest features in the RGS spectrum such as those found at 7.5, 11.4, 15.55, 18.9 and 21.85 Å. Adopting our best-fitting spectral continuum model as template (Table 2, second column), we simulated 10 000 RGS 1 and 2 spectra (accounting for the uncertainties on the continuum parameters). We then added the line as best fitted in our line grid to the continuum model and calculated the changes in the C-statistics (see Fig. 5). For each line, we then computed the number of occurrences where its addition to the continuum-simulated spectra provided an improvement (or Δ C-statistics, with the position of the line free to vary within $\pm 0.2c$ and the continuum parameters also free to vary) larger than that one provided by the line as fitted to the data. This is basically equivalent to create a mock spectrum from the continuum model and search for lines in this spectrum using the same technique adopted in Section 4.2.2. The *p*-values and the corresponding confidence intervals (CI) and sigmas are reported in Table 3. This provides much more conservative limits on the detection. As expected, the blueshifted O VIII line ($\lambda_0 = 18.97$ Å, $\lambda_{obs} \sim 18.90$ Å) is detected well above 3σ, but all the strongest features are still detected above the 99 per cent CI each, even accounting for the look-elsewhere effect.

Although this procedure does not follow exactly all the steps adopted during the line search performed in Section 4.2.2, we acknowledge that it is the best that can be done with the current data. The combined detection of two pairs of strong lines sharing the velocity is certainly encouraging, see also Mg XII–Ne X and O VII–O VIII lines in Fig. 6, but more data are required to place strong constraints.

4.2.4 Simple wind model

We modelled the low-ionization emission lines with a photoionized emission model (PHOTEMIS code imported from XSPEC, which uses XSTAR tables[3]). This model provides a good description of the O VIII resonant line, the O VII k α triplet and the O VII k β line at 18.627 Å ($\log \xi = 1.2 \pm 0.1$), but requires a blueshift of $(0.011 \pm 0.001)c$, i.e. ~ 3000 km s^{-1}. This model provides a significant improvement to the fit with $\Delta \chi^2 / \Delta$ C/dof = 28/27/3 (see also Table 4). We

notice that SPEX calculates the (blue/red) shift of any spectral model according to $E' = E/(1 - v/c)$, which does not account for the relativistic corrections. This was not taken into account in Paper I. Hence, we show all the velocities as defined in SPEX to allow the readers to reproduce our work, but we then use the relativistic formula $z = \sqrt{(1 + v/c)/(1 - v/c)} - 1$ each time we report the blueshift, z, of a certain line or model.

As previously done in Paper I, we modelled the absorption features with the *xabs* model in SPEX. This model calculates the transmission of a slab of material, where all ionic column densities are linked through a photoionization model. The relevant parameter is the ionization parameter $\xi = L/nr^2$, with L the source luminosity, n the hydrogen density and r the distance from the ionizing source (see e.g. Steenbrugge et al. 2003). The equivalent of this model in XSPEC is *warmabs*.[4] Some absorption-like features can be well described with one photoionized *xabs* absorber with a higher ionization parameter ($\log \xi = 3.5 \pm 0.3$) and a relativistic outflow velocity of $(0.16 \pm 0.01)c$, very similar to the $\sim 0.18c$ outflow in NGC 1313 X-1 and NGC 5408 X-1 ($0.2c$ for the non-relativistic correction, see Paper I), see red line in Fig. 6. The absorber reproduces part of the drop below 11 Å and the strong absorption at 16 Å. Several features are however missed by this simple wind model such as the blueshifted Mg XII (8.42 Å) emission line, part of the Fe XXII-XXIII (11.75 Å) – Ne X (12.135 Å) blend and some other absorption like features such as the dip at 15 Å. This suggests that the wind may be more structured. Line widths of 100 km s^{-1} were adopted for all absorption and emission components. A different line width does not improve the fit.

4.2.5 Structured wind model

Multiple emission components – a significant improvement ($\Delta \chi^2 / \Delta$ C/dof = 30/30/3) is obtained if we include another, faster, photoionized emission with $0.082 \pm 0.001c$, which provides an excellent description of the emission features at 7.5 and 11–13 Å (see blue line in Fig. 6 and Table 4). A comparable, slightly worse, fit ($\Delta \chi^2 / \Delta$ C/dof = 25/25/3) is obtained if we instead use a fast collisionally ionized emission component (*cie* in SPEX, *apec* in XSPEC).

Multiple absorption components – the absorption features are less strong and less significant than the emission lines, but we have seen that a single component cannot reproduce all the strongest features. For instance, the troughs between 8.8–10 Å and 15–16 Å or 1.2–1.4 keV and 0.77–0.83, both also seen in EPIC-pn, e.g. Fig. 3. However, adding blindly more absorption components may miss some important features.

First, we considered a wind with a continuous distribution of ionization parameters from 0.2 to 3.8 all at the same velocity. This
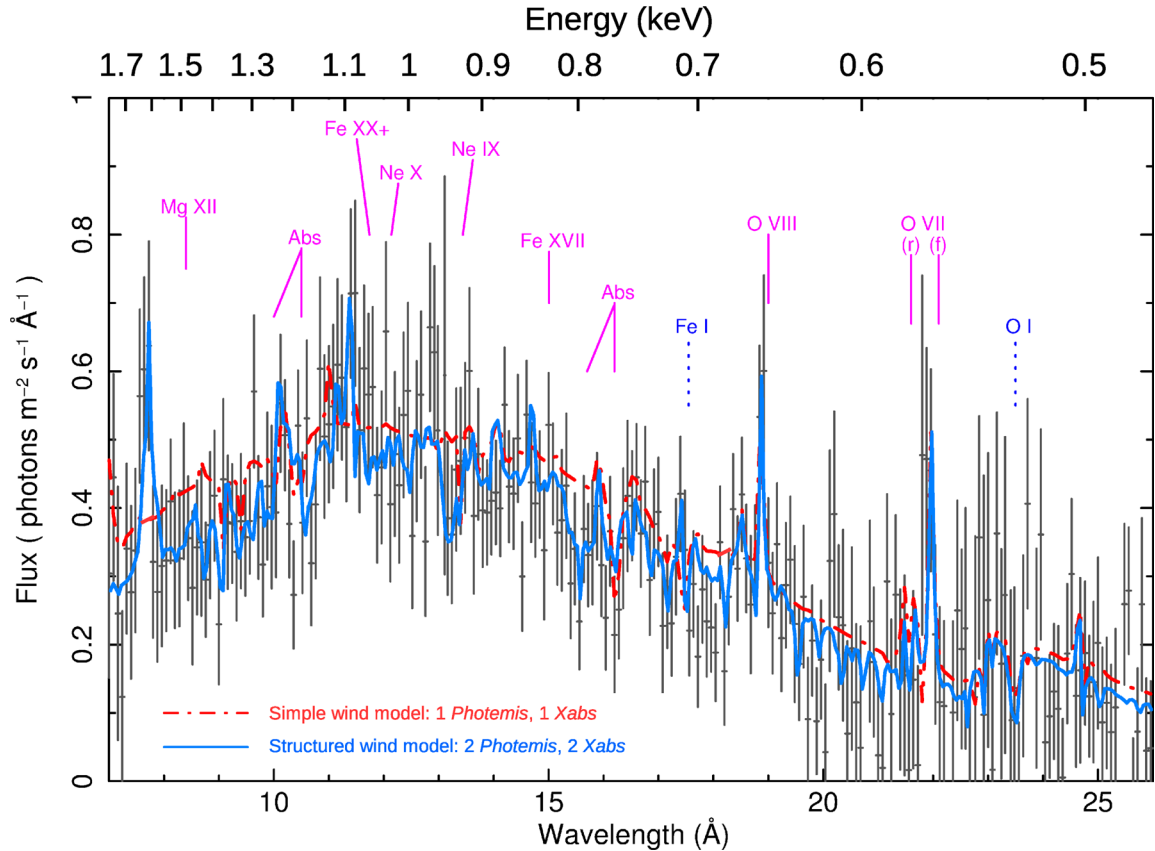
Figure 6. RGS spectrum with two alternative wind models on top of the best-fitting EPIC continuum: the red line has one photoionized outflowing emission (0.01*c*) and one absorption (0.16*c*) components; the blue line has two photoionized emission components (0.01*c* and 0.08*c*) and two absorbers (0.06*c* and 0.20*c*, see Table 4). Rest-frame wavelengths of relevant transitions are labelled. Note the line shift.

Table 4. NGC 55 ULX XMM/RGS fit: main wind components. RGS fits wind components: photoionized emission and photoionized absorption (see also Fig. 6, solid blue line and Fig. 7). The photoionization parameters are in log (ξ, erg cm s^{-1}). Velocities are in units of light speed *c*.

| Parameter	Slow emission	Fast emission	Slow absorption	Fast absorption
$\log \xi$	1.20 ± 0.25	2.80 ± 0.30	0.5 ± 0.3	3.35 ± 0.20
v_{outflow}	0.011 ± 0.001	0.082 ± 0.001	0.058 ± 0.004	0.199 ± 0.003
$\Delta \chi^2 / \Delta\, C$/dof	28/27/3	30/30/3	14/14/3	19/18/3

was done using the *warm* model in SPEX which adopts a continuous distribution of 19 absorbers with a $\Delta\xi$ step of 0.2. This only provided a very small improvement with $\Delta\chi^2$ and $\Delta C = 26$ for 19 new degrees of freedom with respect to the model of continuum plus emission lines. We notice however that the best-fitting outflow velocity of such multi-ionization component is 66 000 km s^{-1}, i.e. 0.2*c* similar to NGC 1313 and NGC 5408 ULX-1. This motivates a different fitting tactic.

The presence of emission lines at different velocities suggests a structured wind and therefore the absorption lines may also exhibit some complex dynamics. To search for a trend of the velocity with the ionization state as well as for some missing components, we created a grid of photoionized absorbers with outflow velocities spanning the 0–0.25*c* range (8 *xabs* components in SPEX with velocity steps of about 10 000 km s^{-1} each). We fit again the RGS data with the EPIC spectral continuum and calculated the improvement in the C-statistics with the addition of each component. There are three degrees of freedom for each absorber: the column density

N_{H}, the ionization parameter ξ and the line-of-sight velocity *v*. The results are shown in Fig. 7.

We found at least two *xabs* components with high significance: ~3σ ($\Delta C/\Delta\chi^2$/dof = 14/14/3) and ~3.5σ ($\Delta C/\Delta\chi^2$/dof = 18/19/3), respectively, at low (~0.5) and high (~3.3) ionization parameters. The low-ξ plasma has a low velocity ~0.06*c*, while the high ξ has relativistically outflowing *v* ~ 0.20*c*. There are several tentative (2σ) detections of material at intermediate velocities, which were broadly reproduced by the single absorber in the simple model used in Section 4.2.4. Interestingly, the ionization parameter of the absorbers seems to show a strong trend with the velocity (see Fig. 7, bottom panel). The effective area of the RGS detector drops dramatically at energies below 1.77 keV (or wavelengths above 7 Å) with a corresponding loss of sensitivity to ionization parameters log $\xi \gtrsim 4.0$. This explains the large error bars at the highest velocities.

In Fig. 8, we show the transmission of the four absorbers with the highest ΔC (8, 8, 14 and 18), which total $\Delta C = 48$ for 12 degrees
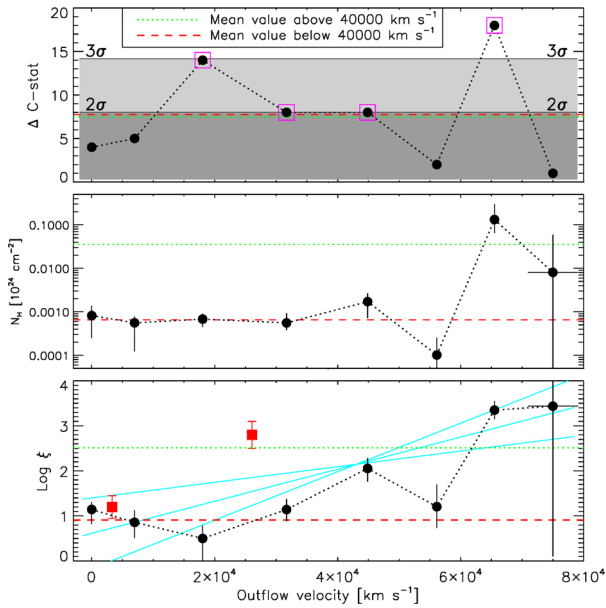
Figure 7. Results of the spectral fits using a grid of eight photoionized absorbers (see Section 4.2.5). The Δ C-statistics indicate the significance of each absorber (each with three degrees of freedom). The column densities, the ionization parameters and the absolute values of the outflow velocities are also shown. The cyan solid lines in the bottom panel show a linear fit with the corresponding 3σ limits. The red filled squares indicate the values of the photoionized emission components (see Table 4). The transmission of the four absorbers indicated by the magenta open squares is shown in Fig. 8. The two absorbers with highest ΔC-statistics are also used in the multiphase wind model shown in Fig. 6 (blue line).
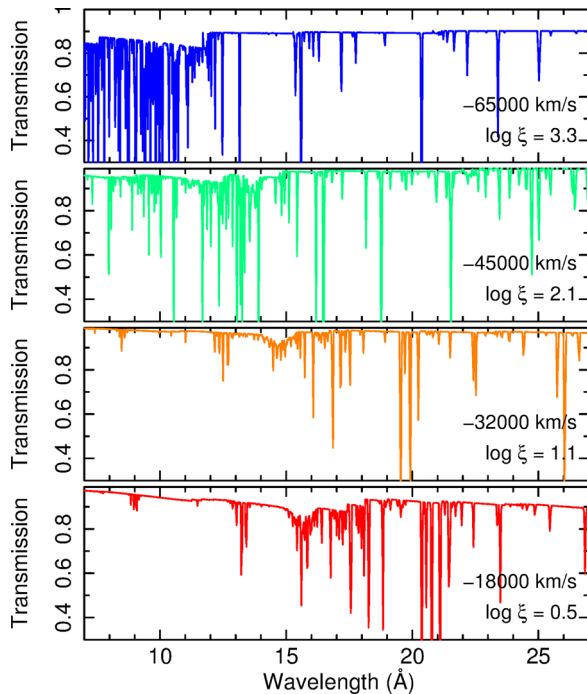
Figure 8. Transmission of the four most relevant absorbers according to a grid of eight photoionized absorbers (see the magenta open squares in Fig. 7). The outflow velocities and the ionization states are labelled. The fastest absorber significantly reduces the flux below 12 Å.

of freedom). This plot is a simple diagnostic tool that shows how the lines shift with the higher outflowing velocities and ionization parameters. We check the effect of a multiphase wind model on the overall spectral fitting by fitting again the RGS spectrum with the two most significant photoionized absorbers ($v \sim 0.06c$ and $\sim 0.20c$) and the two photoionized emitters discussed above on top of the EPIC spectral continuum model. This structured wind model is shown in Fig. 6 (blue line) and provides $\Delta C = 32$ for six degrees of freedom. The model fits the RGS spectrum reproducing most narrow emission and absorption lines such as the drops below 11.5 Å and between 15 and 16 Å. In Table 4, we report the improvements in the fit for these four most significant emission and absorption components. In Appendix A2, we briefly discuss some systematic effects due to the adopted ionization balance.

4.2.6 Do RGS wind components improve EPIC data fits?

A simultaneous fit of RGS and EPIC spectra is not straightforward due to their different characteristics. EPIC-pn has high count rate but low spectral resolution, whilst RGS has low count rate but high spectral resolution. Moreover, there are some cross-calibration uncertainties between them and the energy band of EPIC (0.3–10 keV) is much wider than that of RGS (∼0.35–1.77 keV). However, it is a good exercise to test the wind components from the RGS spectral modelling on to the EPIC data and confirm their existence. Therefore, starting from the EPIC-pn continuum spectral model in Section 4.1 (ID 0655050101), we have added each of the RGS wind components shown in Table 4 on the top of the EPIC double black-body continuum with only the continuum parameters free to vary. We remind that we used χ^2 in the EPIC fits. The addition of the slow low-ξ emitter has a small effect on the fits ($\Delta\chi^2 = 10$) because it is degenerate with the column density at the low spectral resolution of EPIC. The fast high-ξ emitter held $\Delta\chi^2 = 12$. Interestingly, if we use the collisionally ionized RGS solution (see Section 4.2.5) they provide a $\Delta\chi^2 = 15$ each. The introduction of the relativistic (0.2c) photoionized absorber also improves the fits with $\Delta\chi^2 = 27$. The introduction of these components smears out most of the residuals that were detected with a continuum-only model (Fig. 3). The EPIC-pn spectrum provides further support to the results obtained with the RGS only.
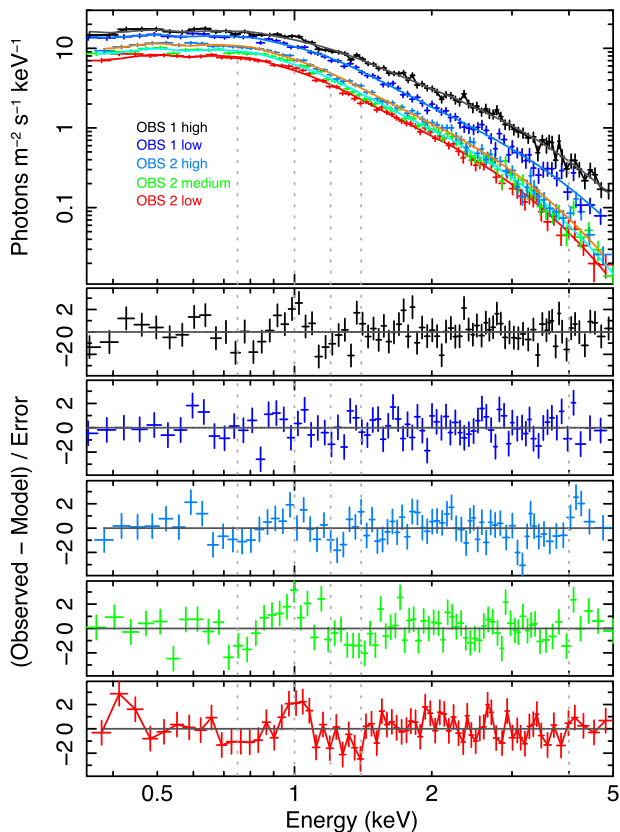
4.3 Flux-resolved spectroscopy

Previous work has suggested that the spectral shape of NGC 55 changes with the source flux: softer when fainter (Stobbart et al. 2004) with the temperatures of the two blackbody components (tentatively) found to be correlated (Pintore et al. 2015). Here, we further investigate this problem using flux-resolved X-ray broadband spectroscopy.

We split the two observations into five flux regimes. A detailed description is provided in Appendix A3. Briefly, we extracted EPIC-pn light curves in the 0.3–10 keV energy band for the two observations, then chose two flux ranges for the first (shorter) observation and three flux ranges for the second observation, and then calculated the good time interval for each flux range. The flux ranges were chosen such that the five spectra extracted in these good time intervals have comparable statistics. The five flux-selected spectra are shown in Fig. 9. A prominent knee appears at 1 keV similar to that seen in some ultraluminous supersoft X-ray sources (e.g. M 101 and NGC 247, Urquhart & Soria 2016).

In a preliminary fit performed to each of the five spectra with the best-fitting $bb+mbb$ continuum model (Section 4.1), we found that

Figure 9. NGC 55 ULX EPIC flux-resolved spectra with a continuum model of blackbody plus modified disc blackbody (see Table 5). The dotted lines show that the residuals could vary.

the column density N_H of the neutral absorber and the temperature of the cooler blackbody T_{bb} did not significantly change between flux-resolved spectra selected from the same observation. We therefore fit simultaneously the spectra of observation 1 coupling the N_H and the T_{bb}. The same coupling was repeated afterwards when simultaneously fitting the spectra of the observation 2.

The flux-resolved spectral fits are shown in Fig. 9. In Table 5, we report the detail of the spectral fits including the observed unabsorbed luminosities. The column density decreases with the increasing luminosity, whilst the temperatures of both the cooler blackbody and the hotter multicolour blackbody increase. The flux-resolved spectra confirm the residuals detected with a higher confidence

in the deeper, stacked, spectrum of the observation 2. Moreover, there is some tentative evidence of variability in the residuals (see Appendix A4). Deeper observations are necessary to study their variability in detail.

5 TIMING ANALYSIS

NGC 55 ULX has shown an interesting temporal evolution in the last decade. Stobbart et al. (2004) found evidence of dips in the light curve, which seem to have significantly smoothed in more recent *Chandra* and *Swift* observations (Pintore et al. 2015). We therefore looked for short- and long-term variations. We extracted the source and background light curves in the same regions used to extract spectra (see Section 3) and obtained a source background-subtracted light curve with the *epiclccorr* task.

5.1 Light curves

NGC 55 ULX light curves are shown in Fig. 10. The light curves were extracted in a soft (0.5–1.0 keV) and a hard (1–5 keV) energy band in order to study the behaviour of the source on the low-energy and high-energy side, respectively, of the 1 keV bump seen in its EPIC spectrum as well as in the spectra of several ULXs (see e.g. Pintore et al. 2015; Urquhart & Soria 2016).

The source behaviour has dramatically changed in the last decade. During the observation of 2001 the hard band was highly variable, exhibiting strong dips as previously shown by Stobbart et al. (2004). During the observation of 2010 the source was much less variable, with the hard and soft band showing the same variability pattern (see Fig. 10). Interestingly, the count rate in 2010 is consistent with the dips observed during the first 2001 observation.

We investigated the variability amplitude in each observation as a function of temporal (Fourier) frequency using power density spectra. We follow the standard method of computing a periodogram in 10 ks light-curve segments before averaging over the segments at each frequency bin, and subsequent binning up over adjacent frequency bins (van der Klis 1989; Vaughan et al. 2003). The resulting power density spectra are shown in Fig. A4 and confirm that the source has very limited variability in 2010 compared to 2001 (see also Heil, Vaughan & Roberts 2009). We therefore focus on the 2001 observation only in the remainder of this section.

5.2 Time lags and covariance spectra

We studied the timing properties of NGC 55 by calculating the cross-spectrum between light curves in different energy bands. A

Table 5. *XMM–Newton*/EPIC broad-band continuum models of flux-resolved spectra.

Component/parameter	OBS 1 high	OBS 1 low	OBS 2 high	OBS 2 medium	OBS 2 low
Flux (10^{-12} erg s^{-1} cm^{-2})	6.74	5.03	3.56	3.06	2.57
L_X (10^{39} erg s^{-1})	3.04	2.27	1.60	1.38	1.16
N_H (10^{21} cm^{-2})	1.45 ± 0.09			2.07 ± 0.08	
L_X (10^{39} erg s^{-1})$_{bb}$	1.23 ± 0.32	1.21 ± 0.28	0.91 ± 0.19	0.80 ± 0.16	0.67 ± 0.14
R (km)$_{bb}$	2320 ± 620	2310 ± 530	3160 ± 650	2960 ± 610	2710 ± 560
kT (keV)$_{bb}$	0.205 ± 0.006			0.163 ± 0.003	
L_X (10^{39} erg s^{-1})$_{mbb}$	1.80 ± 0.24	1.05 ± 0.19	0.69 ± 0.08	0.58 ± 0.07	0.49 ± 0.06
R (km)$_{mbb}$	136 ± 18	121 ± 22	147 ± 16	140 ± 16	132 ± 15
kT (keV)$_{mbb}$	0.931 ± 0.021	0.864 ± 0.025	0.705 ± 0.013	0.691 ± 0.013	0.680 ± 0.013
χ^2/dof	103/89	75/82	84/80	108/81	95/81

Notes. Fluxes and luminosities are estimated between 0.3 and 10 keV. Fluxes are absorbed, whilst luminosities are unabsorbed. The column density N_H of the neutral absorber and the temperature of the blackbody kT_{bb} are coupled between flux-resolved spectra extracted from the same observation. In fact, a preliminary individual fit of each observation provided consistent results.
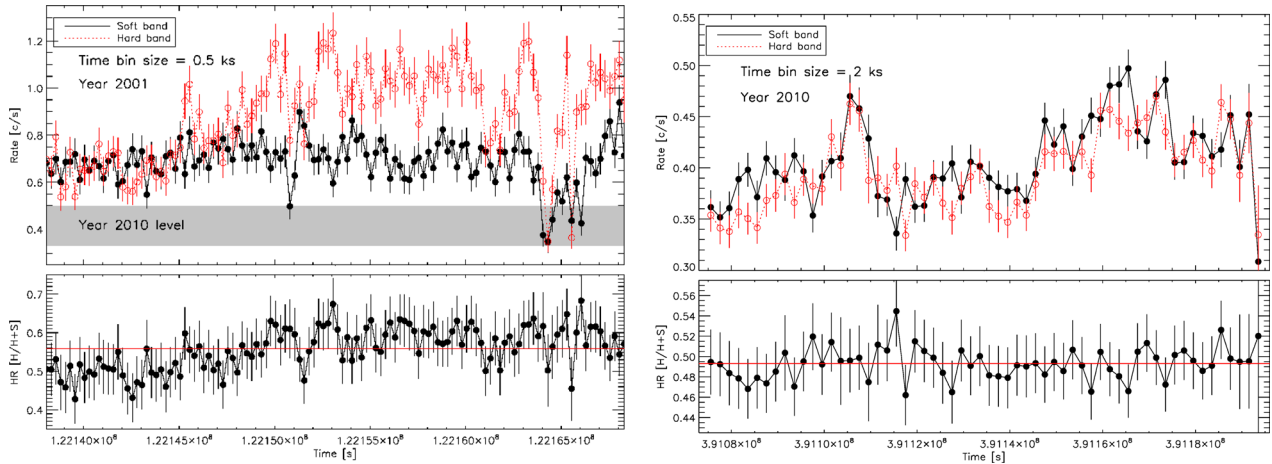
Figure 10. EPIC/pn light curves of the first (left) and second (right) observations, The sizes of the time bins are different between the exposures (500 s and 2 ks) due to the different fluxes. The soft band refers to the 0.5–1 keV energy range and the hard band refers to 1–5 keV. For more detail on the energy band selection see Section 5.1. Notice the lower flux and variability in 2010. The area shaded in grey in the left-hand panel includes the count rate throughout the whole 2010 observation which seems to match the dips seen in 2001.

detailed description of the method can be found in Alston, Vaughan & Uttley (2013) and Uttley et al. (2014, and references therein). We calculated the cross-spectrum at each Fourier frequency in 10 ks segments and then averaged over the segments at each frequency, before binning in geometrically spaced frequency bins by a factor of 1.6. In a given frequency band, we calculated the time lags between a comparison energy band versus a broad (in energy) reference band, whilst subtracting the comparison band from the reference band if it fell within it. In this way, the time lag in each energy bin is the average lag or lead of the band versus the reference band. We used the 0.3–1.0 keV band as reference where the rms is high. In Fig. 11, we show the resulting lag-energy spectrum for three low frequencies.

The power density spectrum is very flat and the Poisson noise dominates above an mHz (see e.g. Heil et al. 2009). We selected three frequency intervals for which it is possible to measure any lag and covariance. Above these frequencies, the lags are consistent with zero and a lot of the covariance energy bins are negative as the noise dominates. We also estimated the lag magnitude expected from the Poisson noise contribution to the phase difference using equation 30 of Vaughan et al. (2003), see red dotted lines in Fig. 11. In the absence of any intrinsic lag, we should expect the bins to be randomly distributed between these limits, which is not the case at least at high and low frequencies.

At low frequencies (0.5–1.5×10^{-4} Hz in Fig. 11 bottom panel) there is evidence for the softer bands lagging behind harder bands. As the frequency increases (from bottom to top panel), there is a systematic change in the lag above 0.9 keV with the profile flattening and possibly the hard bands lagging the soft at higher frequencies (2.5–4.5×10^{-4} Hz). There is a tentative sharp change in the lag below 0.9 keV.

To better understand the behaviour in the lag-energy spectra around 1 keV, we computed the covariance spectra at each Fourier frequency (Wilkinson & Uttley 2009). The covariance spectra show the correlated variability between two energy bands, or between a comparison band and a broad reference band (minus the comparison band). We computed the covariance from the cross-spectrum following Uttley et al. (2014).

The covariance spectra for the same three frequencies are shown in Fig. 12 (top). The overall (mean) covariance spectrum mimics the shape of the energy spectrum (see Fig. 9). The covariance
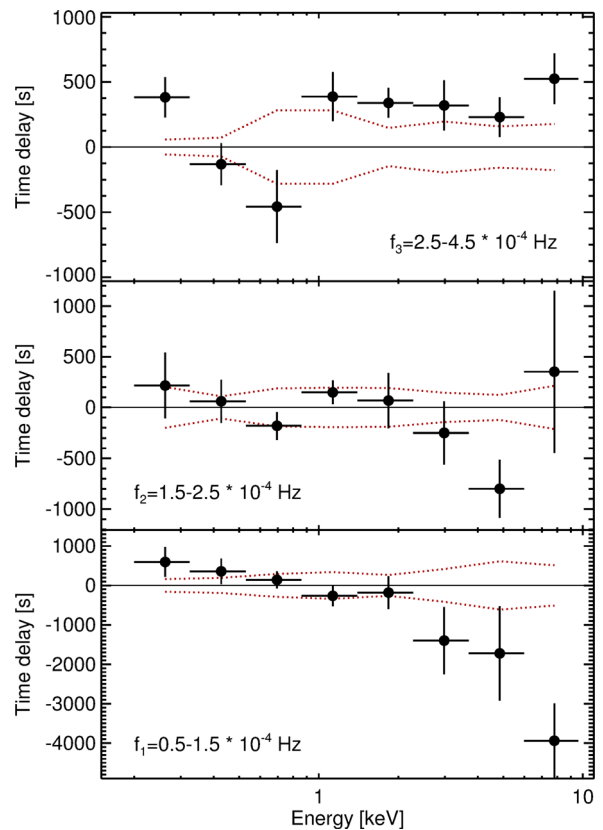
Figure 11. Lag-energy spectra for different frequency ranges with the NGC 55 ULX EPIC-pn (observation 1). Note the trend towards lower energies at low frequencies in the bottom panel. The dotted red lines show the magnitude expected from the Poisson noise. The points should be randomly distributed between these lines in the absence of any lag.

spectra extracted in different frequency ranges follow the trend of the energy lag spectra (see Fig. 11). The covariance increases towards lower energies, but then flattens or possibly drops below 1 keV. On average, the high-frequency covariance spectrum appears to be harder than the low-frequency one, with a possible drop below 1 keV, suggesting the presence of different variability processes
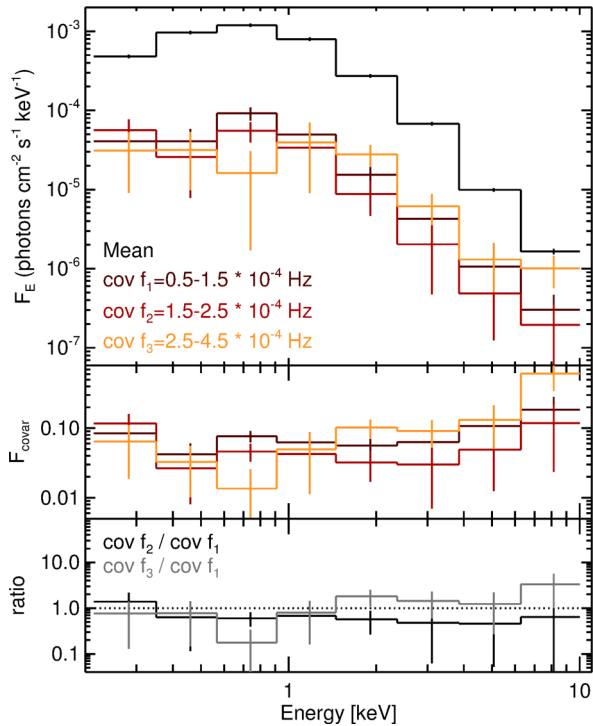
Figure 12. Covariance spectra for the same frequency ranges as Fig. 11 (observation 1). The covariance spectra follow the shapes of the lags measured at the corresponding frequency. The middle panel shows the fractional variability calculated in each frequency range and divided by the mean rate. The bottom panel shows the ratios between the fractional variability at some frequencies.

(Fig. 12 middle panel). The covariance spectra extracted at different frequencies are very similar with the current statistics, but more data would certainly help to distinguish some differences at low and high frequencies. The same applies to the lag-energy spectra. More work will follow up in a forthcoming paper to provide better constraints on these trends and to compare the results with other ULXs.

6 DISCUSSION

Urquhart & Soria (2016) modelled the soft X-ray spectral features and the ∼ 1 keV (∼12 Å) drop in several CCD spectra of ULSs with a model of thermal emission and an absorption edge. They interpreted the features as a result of absorption and photon reprocessing by an optically thick wind which obscures the innermost regions where most hard X-rays are produced. This suggested that ULSs are actually ULXs viewed almost edge on or maybe their outflow is thicker, at the same viewing angle. A denser, more optically thick outflow may be the result of higher accretion rates above Eddington, assuming that $\dot{M}_{\text{wind}}$ is proportional to $\dot{M}_{\text{disc}}$ (e.g. Shakura & Sunyaev 1973). Moreover, at higher super-Eddington rates, the outflow launching region moves to larger radii on the disc, where the escape velocity and the Compton temperature are lower, which favours denser winds (e.g. Poutanen et al. 2007). Motivated by the recent detection of relativistic winds in the NGC 1313 and NGC 5408 ULX-1 high-resolution RGS spectra taken with *XMM–Newton* (see Paper I), we searched for a deep RGS observation of an object that shows the properties of both the ULX and ULS states and found NGC 55 ULX.

6.1 Discovery of a powerful wind

The primary goal of our study was the search for unambiguous signatures of a wind. The detection of (unresolved) spectral residuals in previous work done on NGC 55 ULX was certainly encouraging (e.g. Middleton et al. 2015b). We confirmed the presence of these residuals particularly in the 2010 EPIC deep spectrum (see Figs 3 and 9).

The evidence hinting at a wind was confirmed when we looked at the high-resolution RGS spectrum of NGC 55 ULX, which shows a wealth of emission and absorption features located at energies that are blueshifted compared to the energies of the strongest atomic transitions in the soft X-ray energy band (see Figs 4 and 5). Accurate spectral modelling shows the presence of an outflowing plasma with a complex ionization and velocity structure (see Figs 6 and 7). The best-fitting models suggest photoionization, but we cannot exclude some contribution from the collisional ionization, particularly for high-ionization species. The gas responsible for the emission lines moves with velocities (0.01–0.08)c lower than those exhibited by the absorbing gas (0.06–0.20)c, see Table 4 and Fig. 7. Both the emission and the absorption lines indicate that the ionization state increases with the outflow velocity suggesting that we are detecting hotter/faster phases coming from inner regions. Our limited statistics prevents us from claiming the detection of more than two photoionized emitters and absorbers in the line of sight, but additional observations would certainly help to understand the ionization and velocity structure of the wind in NGC 55 ULX.

An interesting result is the spectral signature of the high-ionization (log $\xi \sim 3.3$) absorber with the largest column density. This component absorbs a substantial amount of photons below 12 Å (or above 1 keV), which provides a natural explanation for the spectral shape of NGC 55 ULX and the drop seen in several ULSs (e.g. Urquhart & Soria 2016). The main difference is that such a turnover is more pronounced in ULSs because they are seen more edge on or because the photosphere of the wind is simply further out due to a larger accretion rate (see e.g. Middleton et al. 2015a; Urquhart & Soria 2016) with resulting increased obscuration of the inner regions.

It is useful to compare the wind power to the bolometric radiative luminosity of the source. The kinetic luminosity of the outflow or wind power $L_{\text{kin}} = 1/2\dot{M}v_{\text{out}}^2$ can be expressed as $L_{\text{kin}} = 2\pi L_{\text{ion}} m_{\text{p}} \mu v_{\text{out}}^3 C_V \Omega/\xi$, where L_{ion} is the ionizing luminosity, m_{p} is the proton mass, μ is the mean atomic weight (∼1.2 for solar abundances), v_{out} is the outflow velocity, C_V is the volume filling factor (or 'clumpiness'), Ω is the solid angle and ξ is the ionization parameter of the wind. We calculated the ratio between the wind power and the bolometric luminosity for the fast and most significant absorber (see Table 4) and obtained: $L_{\text{kin}}/L_{\text{bol}} = 1300 \pm 650 C_V \Omega L_{\text{ion}}/L_{\text{bol}}$. According to the simulations of Takeuchi et al. (2013), a wind driven by a strong radiation field in super-Eddington accretion has a typical clumpiness factor of ∼0.3 and is launched over wide angles of 10°–50° from the disc rotation axis. A significant fraction of the source radiative luminosity (L_{bol}) must have been used to ionize the wind before some reprocessing occurred. In our broad-band EPIC fits we found that, on average, the 0.3–10 keV total source flux was equally partitioned between the hard (disc) and soft (reprocessed) components. Therefore, it is reasonable to adopt $L_{\text{ion}}/L_{\text{bol}} \sim 0.5$. This provides $L_{\text{kin}}/L_{\text{bol}} \sim 30$–100, which is similar to that measured for NGC 1313 X-1 and NGC 5408 X-1 (see Paper I; Walton et al. 2016a), but is an extreme value if compared to the strongest outflows seen from sub-Eddington systems, e.g. active galactic nuclei (e.g. Fabian 2012, and references therein).

6.2 Long- and short-term spectral variability

We studied the timing and spectral properties of NGC 55 ULX to understand if they also suggest that the source is a transition between classical ULXs and ULSs.

If the thick, outflowing, wind scenario is correct then we should expect a correlation between the spectral hardness of the source and the X-ray flux (e.g. within 0.3–10 keV). For instance, if either the accretion rate or the inclination decreases then the optical depth decreases, which corresponds to a lower down-scattering of the hard photons produced in the inner regions. We test this picture by splitting the observations in different flux regimes which provided five high-quality EPIC spectra (see Fig. 9). We modelled the EPIC spectra with a spectral continuum consisting of a blackbody and a multicolour blackbody emission components in agreement with Pintore et al. (2015) and with our search for the best-fitting continuum. The temperatures of both components (particularly the hotter multicolour blackbody) significantly increase with the luminosity supporting the wind scenario (see Table 5). This is confirmed by the observed decrease in column density of the neutral absorber with luminosity (the Galactic interstellar medium account less than 10 per cent according to the H I maps and does not affect our result). In support for this scenario, we also found that the emitting area of the soft (~0.2 keV) blackbody component increased by a factor 2 from the brighter (2001) to the fainter (2010) observation in agreement with the study of ULSs of Urquhart & Soria (2016) and Feng et al. 2016, where the expansion of the photosphere and the decrease of the temperature shift the peak of the spectrum from the X-ray to the far-UV energy band. According to our spectral fits, the radius of the photosphere is 2000–3000 km and the temperature well above 0.15 keV, which explains why NGC 55 still looks like ULX rather than a ULS according to the classifications of Sutton et al. (2013) and Urquhart & Soria (2016). This may suggest that either the inclination or the accretion rate in NGC 55 is smaller than in typical ULSs.

There are no striking dips in the 2010 exposure if compared to those in 2001, which is not surprising since they were not detected in most recent observations taken with *Chandra* and *Swift* (see Pintore et al. 2015). Light curves extracted with the same binning are shown in Appendix A3. We remark that the flux level in 2010 is consistent with the lowest level of 2001, suggesting that the source is in a semi-obscured state (see Fig. 10). The lack of variability and the low flux in 2010 is consistent with a picture where the innermost regions, which produce the high-energy hard X-rays and the high variability, are partly obscured by an intervening absorber in agreement with the hypothesis of Stobbart et al. (2004), Middleton et al. (2011) and Sutton et al. (2013). Either the accretion rate increased, further inflating the outer regions of the disc, or the line of sight changed (e.g. due to precession) with further obscuration of the innermost 'hotter' regions.

The tentative detection of a large soft lag, ~1000 s, at low frequencies further strengthens our scenario (see Fig. 11) suggesting that the soft emitting gas in the wind and the upper disc photosphere are reprocessing the photons produced in the innermost regions. The covariance spectra computed within different frequency ranges follow the shape of the lag-energy spectra (see Fig. 12), confirm this picture and show evidence for two possible main processes that produce variability: fluctuation within the inner disc (harder) and slow reprocessing through the wind (softer). It is also possible that when the column density of the wind decreases the wind becomes optically thin, but the hard X-ray photons start penetrating the wind before the soft photons (see e.g. Kara et al. 2015). This may explain

the source hardening when the luminosity increases. In a future project, we will investigate all possible scenarios by comparing more sources and lags at different time-scales.

Our results agree with Middleton et al. (2015a). They computed the covariance spectra on a broad frequency band and showed a significant lack of variability in the 2010 observation, suggesting that the variable, hard, X-ray component has intercepted cooler/optically thicker material. They also found that the shape of the covariance spectra in NGC 55 ULX and several other ULXs was consistent with the variability originating in the hard component only, which agrees with a model where the variability on short and long time-scales at moderate inclinations is dominated by obscuration of the high-energy emission.

The lags tentatively detected here appear at much lower frequencies than those shown by Heil & Vaughan (2010) and De Marco et al. (2013) in NGC 5408 X-1. Hernández-García et al. (2015) also found evidence of a ~ 1 ks time lag in NGC 5408 X-1 and showed that the time delays are energy dependent and that their origin is not related to reflection from an accretion disc (reverberation). They also argued that associating the soft lag with a quasi-periodic oscillation (QPO) in these ULXs, drawing an analogy between soft lags in ULXs and soft lags seen in some low-frequency QPOs of Galactic X-ray binaries, is premature.

The two orders of magnitude in time delays (from a few seconds to hundred seconds in NGC 55 and NGC 5408 ULXs) point towards a complex energy lag spectrum and we also caution from using lags to derive mass estimates without a comprehensive analysis in a large frequency range. Although this is beyond the scope of this paper, we provide a simple argument to compare lags in AGN, X-ray binaries and ULXs. The lag magnitude in NGC 55 ULX as a function of the variability time-scale is ~10 per cent (1000 s; $1/f = 10\,000$ s). The hard lags in AGN are typically 1 per cent, the AGN soft lags are ~2 per cent (e.g. Alston et al. 2013), whilst in hard state X-ray binaries they are 0.5–1 per cent (e.g. Uttley et al. 2011). De Marco et al. (2013) measured about ~5 per cent for the higher frequency lags in NGC 5408 X-1. Hence, it is possible that the processes causing these lags are different. The long soft lags in NGC 55 ULX and NGC 5408 X-1 could be related to some phenomena occurring in the outer region. In fact, the 1000 s magnitude is likely due to the combination of light travel time plus thermalization in the wind and additional local scattering processes before the photons are re-emitted towards the observer. Such phenomena imply a distance that can be large enough to damp the variability with a corresponding decreasing of the covariance at high frequencies (see Fig. 12). The short (a few seconds) soft lags seen by Heil & Vaughan (2010) and De Marco et al. (2013) can be different processes occurring in the inner regions.

6.3 NGC 55 versus ULXs and ULSs: the big picture

A lot of work has already been done in order to classify ULXs and ULSs and to understand the effect of the inclination (viewing angle) and the accretion rate on their spectral and timing behaviour (see e.g. Gladstone et al. 2009; Sutton et al. 2013; Middleton et al. 2015; Urquhart & Soria 2016, and references therein). Therefore, we briefly highlight why NGC 55 ULX looks like a transitional form between ULXs and ULSs for the shape of its spectral continuum. More attention will be given on the way the detection of winds fits in the framework of super-Eddington accretion.

6.3.1 The spectral shape

The higher energy broad-band component is an interesting link between ULXs and ULSs. The sequence from hard ULXs to soft

ULXs and then to ULSs shows a progressively lower temperature (whether modelled as Comptonization or a modified disc, e.g. Gladstone et al. 2009). The temperature is therefore a function of $\dot{M}_{wind}$ and/or the viewing angle. The optical depth τ (for a Comptonization model) instead increases along the same sequence, from $\tau \sim$ few for hard ULXs to $\tau \gtrsim 10$ for soft ULXs, to $\tau \longrightarrow$ infinity for ULSs. Alternatively, the photon index Γ increases from $\sim$1.5 to $\sim$2.5 and then >4 along the same sequence in analogy with the (T, τ) changes for a Comptonizing region. The hard component of NGC 55 can be well modelled as either a steep ($\Gamma > 4$) power law or as a modified disc, which essentially means a large τ (see e.g. Tables 2 and 5). We have also shown that the shape of NGC 55 ULX spectrum matches that of the high-flux state of NGC 247 ULX, an object that shifts between the ULX and the ULS classical states (see Fig. 1). This suggests that NGC 55 ULX is indeed a transitional object between the ULXs and ULSs.

6.3.2 The spectral features

The emission and absorption features detected in NGC 55 ULX are produced by the same ionic species detected in NGC 1313 X-1 and NGC 5408 X-1 RGS spectra (see Paper I). For instance, the properties of the most significant absorber detected in NGC 55 ULX (see e.g. Table 4) seem to match those of the fast (0.2c) component in the other two ULXs. The detection of a multiphase structure in NGC 55 ULX would point towards a tighter analogy to NGC 5408 X-1, which also exhibits a wind more complex than NGC 1313 X-1, with different ionization states and outflow velocities. We notice that evidence for an edge-like feature around 11 Å was also found in the RGS spectrum of NGC 6946 X-1 (see Paper I), which sometimes exhibits very soft spectra like NGC 55 and NGC 5408 (the SUL regime, Sutton et al. 2013). Unfortunately the interpretation of this feature in NGC 6946 X-1 was difficult due to its flux at 1 keV (OBS ID 0691570101) $\sim$50 per cent lower than NGC 55 ULX.

The presence of *blueshifted* emission lines in NGC 55 ULX suggests that we may be looking through a different line of sight compared to NGC 1313 and 5408 ULXs. The continuum is for instance significantly lower than NGC 5408 X-1 (see Extended Data fig. 4 in Paper I), but at 1 keV NGC 55 ULX is comparable if not brighter, with the emission lines at other energies also matching the flux of the lines in the other ULXs. Remarkably, the line-emitting gas phases account for 10–20 per cent of the total source flux in the X-ray (0.2–10 keV) energy band in agreement with NGC 5408 X-1, while in NGC 1313 X-1 the lines contribute about 5 per cent of the source flux. If the emission lines in these ULXs have the same origin then we should expect that NGC 55 ULX is seen through a preferential line of sight where the outflow velocity of the emission component is almost maximum (see Fig. 13), while the other three ULXs may be seen through a line of sight where the motion of the line-emitting gas is more tangential. This would explain why the emission lines in NGC 5408 X-1 appear to be broader by an order of magnitude ($\sigma_v \sim 1000$ km s^{-1}, see Paper I).

NGC 1313 X-1 shows a large range of spectral hardness with strong absorption features at $\sim$0.2c, which suggests moderate inclination angles with the wind variability possibly due to precession (see Middleton et al. 2015b). Holmberg IX X-1 shows very shallow residuals in EPIC spectra and a spectral hardness among the highest measured in ULXs which argues in favour of a nearly face on view (e.g. Sutton et al. 2013; Middleton et al. 2015a; Luangtip, Roberts & Done 2016; Walton et al. 2016b).

The emission features detected in NGC 55 ULX are produced by the same ionic species that give origin to the blueshifted emission
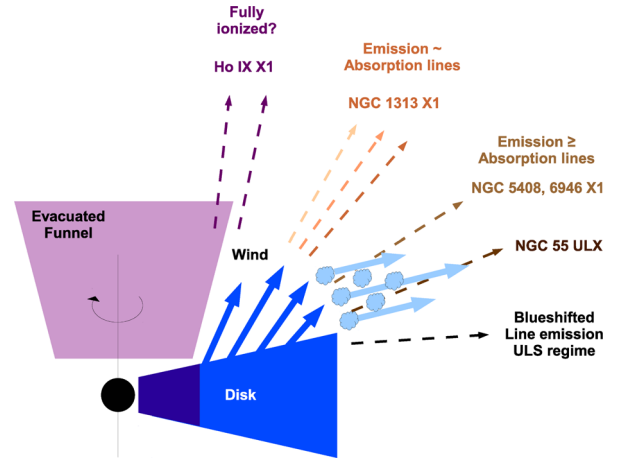

Figure 13. Simplified scheme of high-mass accretion rate sources (see also Middleton et al. 2011). The light blue region shows the soft X-ray emission of the accretion disc, altered by a photosphere of a radiatively driven optically thick wind. The dark blue region, closer to the compact object is dominated by highly variable, optically thinner, turbulent Comptonization emitting high-energy (>1 keV) X-rays. The dashed lines indicated some possible sightlines for some famous ULXs and for the ULS regime (see e.g. Urquhart & Soria 2016). We believe that the line of sight of NGC 55 ULX is somewhere between the classical ULX and ULS sources, but still at high inclination where outflowing material is both emitting and absorbing photons from the inner regions.

detected in the relativistic jet of the Galactic super-Eddington accretor SS 433 (see e.g. Marshall, Canizares & Schulz 2002, and references therein). Similar, powerful, outflows have been discovered in Galactic black holes X-ray binaries such as IGR J17091−3624 (King et al. 2012), MAXI J1305−705 (Miller et al. 2014), 4U 1630−47 (Diaz-Trigo et al. 2012) and during superburst of the neutron star X-ray binary SAX J1808.4−3658 (Pinto et al. 2014).

6.3.3 Ultraluminous supersoft sources

A comprehensive analysis of the ULX phenomenology also needs high-resolution spectroscopy of ULSs in order to study the cases of extreme absorption and to ultimately confirm an unification scenario for ULXs and ULSs (see Fig. 13 and e.g. Poutanen et al. 2007; Urquhart & Soria 2016, and references therein). The ULS archive has *XMM–Newton* exposures that are just too short ($\lesssim$50 ks) to provide RGS spectra with statistics good enough to significantly detect sharp spectral features. NGC 247 ULX is likely the best candidate among all ULSs because of its brightness, good isolation and sharp drop at 1 keV (see e.g. Feng et al. 2016; Urquhart & Soria 2016). The RGS archive has two on-axis exposures with a modest 30 ks exposure time each. These prevent us from doing an accurate analysis, particularly for the low-flux ULS spectrum, which would require more data or additional spectra of other ULSs and, therefore, we defer this work to future work.

Here, we present a preliminary result. Briefly, we repeated the RGS analysis done in this work on NGC 55 ULX with the high-flux RGS exposure of NGC 247 ULX (ID 0728190101, see Section 2). The spectrum also shows hints for absorption and emission features, fainter than in NGC 55 ULX due to the worse statistics (see Fig. 14). In particular, RGS confirms the spectral bending below 12 Å (above 1 keV) as seen in CCD spectra (see Fig. 1). It is encouraging that the spectral features can be modelled with a wind model similar to that used in NGC 55 ULX, i.e. two photoionized emitters and one photoionized absorber, with the ionization increasing with the outflow
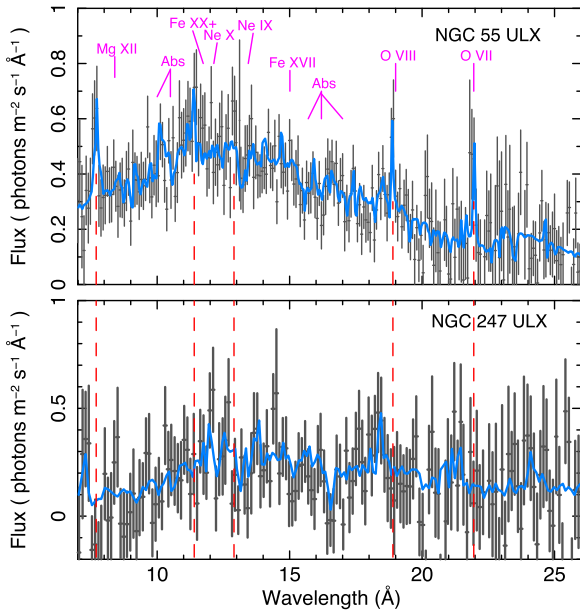
Figure 14. NGC 55 ULX RGS spectrum with the overlaid structured model (top) compared to NGC 247 ULX with a similar wind model on top of a blackbody emission continuum (bottom): low-ξ slow ($v = 0.05c$) and high-ξ fast ($v = 0.13c$) photoionized emission components and high-ξ fast ($v = 0.14c$) photoionized absorption. The red dashed lines mark some relevant blueshifted emission line detected in NGC 55 ULX. Some interesting features appear on their blue side in NGC 247 ULX.

velocity (see Fig. 14). The velocity of the line emitters in NGC 247 ULX seems to be even higher than those in NGC 55 ULX showing a further preferential location of the line of sight. Jin et al. (2011) have analysed the ULS-state EPIC-pn spectrum of NGC 247 that we have shown in Fig. 1 and found similar residuals to those detected in NGC 55 ULX. In particular, absorption features at 0.7 and above 1 keV as well as emission at or just below 1 keV. As suggested by Feng et al. (2016) and Urquhart & Soria (2016), the supersoft ultra-luminous (SSUL or ULS) regime is likely an extension of the SUL state towards higher high accretion rates with the blackbody emission arising from the photosphere of thick outflows and the hard X-rays being emission leaked from the embedded accretion disc via the central low-density funnel or advected through the wind. The wind thickens throughout the ULX–SUL–SSUL sequence and imprints the spectral curvature and the absorption edge at 1 keV.

6.4 *XMM–Newton* in the next decade

Ideally, we would need a statistical sample to probe the scenario shown in Fig. 13 comparing the properties of the wind in sources at different angles of inclination to the observer and mass accretion rate. Only a handful of sources have been observed with deep, on-axis, *XMM–Newton* observations with statistics good enough to enable RGS analysis and no on-axis full-orbit observation of any bright ULS has ever been taken. The fact that the wind lines can be studied imply that with a long exposure of a ULS we will learn more about their physics. Deeper observations of other ULXs and ULSs will provide a complete sample of ultrafast winds, while deeper observations of those sources which already have well-exposed RGS spectra (e.g. NGC 1313 X-1 and NGC 55 ULX) will enable to study the wind in detail and its dependence on flux, spectral hardness and source quasi-periodicities (e.g. Walton et al. 2016a). All this is crucial to understand the relation between the wind and

both the accretion rate and the viewing angle, which is useful to understand the launching mechanism.

This research field is still rather new and the ESA's *XMM–Newton* satellite has unique capabilities to further develop it. The gratings on board NASA's *Chandra* satellite (High-Energy Transmission Grating (HETGS)/Low Energy Transmission Grating Spectrometers (LETGS), e.g. Brinkman et al. 2000; Canizares et al. 2005) have the highest spectral resolution available in the X-ray band, but their effective area is smaller than that of RGS in the soft X-ray band where most ULX wind features are shown and where the flux is highest. HETGS and LETGS are clearly optimal to distinguish spectral features in the brightest objects, whilst the RGS has unique capabilities to detect lines in weak objects, which means that the continuation of the *XMM–Newton* and *Chandra* missions is crucial to study the ULXs and ULSs in detail.

ULXs and ULSs will be excellent targets for a *Hitomi* replacement mission, for the proposed *Arcus* gratings mission and, particularly, for the two-square-metre ESA's *Athena* mission. *Arcus* can significantly improve the RGS results due its much higher spectral resolution in the soft X-ray energy band (e.g. Kaastra 2016). *Hitomi* has already proven that we can change the way we perform X-ray spectroscopy thanks to its combination of excellent spectral resolution and collective area in the high-energy X-ray band (Hitomi Collaboration 2016). *Athena* will completely revolutionize X-ray astronomy due to its combination of high spatial and spectral resolution (Nandra et al. 2013).

We remark that the study of the accretion flow in ULXs and ULSs is important to understand the phenomenology of super-Eddington accretion, which may be required to occur during the early stages of the Universe to build up the supermassive black holes that have been discovered to power AGN at high redshifts (see e.g. Volonteri et al. 2013).

7 CONCLUSIONS

In the last decade it has been proposed that a substantial fraction of the population of ULXs and ultraluminous supersoft sources (ULSs) are powered by super-Eddington accretion on to compact objects such as neutron stars and black holes (see e.g. King et al. 2001; Roberts 2007; Feng et al. 2016; Urquhart & Soria 2016, and references therein). In particular, ULSs could be a category of ULXs observed at high inclination angles, possibly edge on, where a thick layer of material is obscuring the innermost hard X-ray emitting regions (e.g. Kylafis & Xilouris 1993; Poutanen et al. 2007). We have studied the NGC 55 ULX that we believe is a hybrid source showing properties common to both ULX and ULS. The presence of a spectral curvature at 1 keV and a high-energy tail that can be described as a $\gtrsim 0.7$ keV disc-like blackbody places it just in between these two categories of X-ray sources.

We have found a powerful wind characterized by emission and absorption lines blueshifted by significant fractions of the speed of light (0.01–0.20c) in the *XMM–Newton*/RGS spectrum of NGC 55 ULX. The detection of such a wind is consistent with the predictions of super-Eddington accretion (Takeuchi et al. 2013). The wind has a complex dynamical structure with an ionization state that increases with the outflow velocity, which indicates launching from different regions of the accretion disc. The comparison of the wind in NGC 55 ULX with that detected in other ULXs (Paper I) suggests that the source is being observed at high inclinations, but not high enough to look exactly like a ULS, in agreement with the classification on the basis of its spectral shape (e.g. Sutton et al. 2013). However,

the strongest wind component partly absorbs the source flux below 1 keV, generating a drop similar to that observed in ULSs.

The long- and short-term spectral variability of the source shows a softening of the spectrum at lower luminosities, i.e. around the Eddington luminosity (for a 10 M$_\odot$ black hole), which agrees with the proposed scenario of wind clumps crossing the line of sight and partly obscuring the innermost region where most hard X-rays come from (e.g. Middleton et al. 2015a, and references therein).

We have found evidence for a long ∼1000 s soft lag at low frequencies, similar to NGC 5408 X-1 (Hernández-García et al. 2015), which may indicate that part of the emission coming from the inner regions has been reprocessed in the outer regions before being re-emitted towards the observer. This provides further support to the wind scenario.

Deeper *XMM–Newton* observations of NGC 55 ULX and other ULXs and ULSs will enable a detailed study of the dependence of the wind on the accretion rate and the inclination angle, which can help us to understand the geometry and the accretion flow in these extraordinary astronomical objects and in super-Eddington accretors in general.

ACKNOWLEDGEMENTS

REFERENCES

Alston W. N., Vaughan S., Uttley P., 2013, MNRAS, 435, 1511
Bachetti M. et al., 2014, Nature, 514, 202
Brinkman B. C. et al., 2000, in Truemper J. E., Aschenbach B., eds, Proc. SPIE Conf. Ser., Vol. 4012, X-Ray Optics, Instruments, and Missions III. SPIE, Bellingham, p. 81
Canizares C. R. et al., 2005, PASP, 117, 1144
De Marco B., Ponti G., Miniutti G., Belloni T., Cappi M., Dadina M., Muñoz-Darias T., 2013, MNRAS, 436, 3782
den Herder J. W. et al., 2001, A&A, 365, 7
Di Stefano R., Kong A. K. H., 2003, ApJ, 592, 884
Di Stefano R., Kong A. K. H., 2004, ApJ, 609, 710
Díaz Trigo M., Miller-Jones J. C. A., Migliari S., Broderick J. W., Tzioumis T., 2012, Nature, 504, 260
Elvis M., 2000, ApJ, 545, 63
Fabian A. C., 2012, ARA&A, 50, 455
Farrell S. A., Webb N. A., Barret D., Godet O., Rodrigues J. M., 2009, Nature, 460, 73
Feng H., Tao L., Kaaret P., Grise F., 2016, ApJ, 831, 117
Fuerst F. et al., 2016, ApJ, 831, 14
Gladstone J. C., Roberts T. P., Done C., 2009, MNRAS, 397, 1836
Greene J. E., Ho L. C., 2007, ApJ, 656, 84
Heil L. M., Vaughan S., 2010, MNRAS, 405, L86
Heil L. M., Vaughan S., Roberts T. P., 2009, MNRAS, 397, 1061
Hernández-García L., Vaughan S., Roberts T. P., Middleton M., 2015, MNRAS, 453, 2877
Hitomi Collaboration, 2016, Nature, 535, 117
Israel G. L. et al., 2017a, Science, 355, 817
Israel G. L. et al., 2017b, MNRAS, 466, L48
Jin J., Feng H., Kaaret P., Zhang S.-N., 2011, ApJ, 737, 87
Kaastra J. S., 2016, in XMM-Newton: The Next Decade. Available at: http://www.cosmos.esa.int/web/xmm-newton/2016-workshop
Kaastra J. S., Bleeker J. A. M., 2016, A&A, 587, 151
Kara E. et al., 2015, MNRAS, 446, 737
King A. R., Davies M. B., Ward M. J., Fabbiano G., Elvis M., 2001, ApJ, 552, L109
King A. L. et al., 2012, ApJ, 746, L20
Kong A. K. H., Di Stefano R., 2003, ApJ, 590, L13
Kylafis N. D., Xilouris E. M., 1993, A&A, 278, 43
Liu J.-F., Bregman J. N., Bai Y., Justham S., Crowther P., 2013, Nature, 503, 500
Luangtip W., Roberts T. P., Done C., 2016, MNRAS, 460, 4417
Lumb D. H., Warwick R. S., Page M., De Luca A., 2002, A&A, 389, 93
Marshall H. L., Canizares C. R., Schulz N. S., 2002, ApJ, 564, 941
Mezcua M., Civano F., Fabbiano G., Miyaji T., Marchesi S., 2016, ApJ, 817, 20
Middleton M. J., Roberts T. P., Done C., Jackson F. E., 2011, MNRAS, 411, 644
Middleton M. J. et al., 2013, Nature, 493, 187
Middleton M. J., Walton D. J., Roberts T. P., Heil L., 2014, MNRAS, 438, 51
Middleton M. J., Heil L., Pintore F., Walton D. J., Roberts T. P., 2015a, MNRAS, 447, 3243
Middleton M. J., Walton D. J., Fabian A., Roberts T. P., Heil L., Pinto C., Anderson G., Sutton A., 2015b, MNRAS, 454, 3134
Miller J. M. et al., 2014, ApJ, 788, 53
Nandra K. et al., 2013, preprint (arXiv: 1306.2307)
Pinto C., Ness J.-U., Verbunt F., Kaastra J. S., Costantini E., Detmers R., 2012, A&A, 543, 134
Pinto C., Kaastra J. S., Costantini E., de Vries C., 2013, A&A, 551, 25
Pinto C., Costantini E., Fabian A. C., Kaastra J. S., in't Zand J. J. M., 2014, A&A, 563, 115
Pinto C., Middleton M. J., Fabian A. C., 2016, Nature, 533, 64 (Paper I)
Pintore F., Esposito P., Zampieri L., Motta S., Wolter A., 2015, MNRAS, 448, 1153
Porquet D., Dubau J., 2000 A&AS, 143, 495
Poutanen J., Lipunova G., Fabrika S., Butkevich A. G., Abolmasov P., 2007, MNRAS, 377, 1187
Roberts T. P., 2007, Ap&SS, 311, 203
Shakura N. I., Sunyaev R. A. M., 1973, A&A, 24, 337
Soria R., Kong A. K. H., 2016, MNRAS, 456, 1837
Steenbrugge K. C., Kaastra J. S., de Vries C. P., Edelson R., 2003, A&A, 402, 477
Stobbart A.-M., Roberts T. P., Warwick R. S., 2004, MNRAS, 351, 1063
Stobbart A.-M., Roberts T. P., Wilms J., 2006, MNRAS, 368, 397
Sutton A. D., Roberts T. P., Middleton M. J., 2013, MNRAS, 435, 1758
Sutton A. D., Roberts T. P., Middleton M. J., 2015, MNRAS, 814, 73
Takeuchi S., Ohsuga K., Mineshige S., 2013, PASJ, 65, 88
Turner M. J. L. et al., 2001, A&A, 365, 27
Urquhart R., Soria R., 2016, MNRAS, 456, 1859
Uttley P., McHardy I. M., 2001, MNRAS, 323, 26
Uttley P., Cassatella P., Wilkinson T., Wilms J., Pottschmidt K., Hanke M., Böck M., 2011, MNRAS, 414, 60
Uttley P., Cackett E. M., Fabian A. C., Kara E., Wilkins D. R., 2014, A&AR, 22, 72
van der Klis M., 1989, ARA&A, 27, 517
Vaughan S., Edelson R., Warwick R. S., Uttley P., 2003, MNRAS, 345, 1271
Volonteri M., Sikora M., Lasota J.-P., Merloni A., 2013, ApJ, 775, 94
Walton D. J. et al., 2016a, ApJ, 826, 26
Walton D. J. et al., 2016b, ApJ, 827, 13
Webb N. et al., 2012, Science, 337, 554
Wilkinson T., Uttley P., 2009, MNRAS, 397, 666

APPENDIX A: SYSTEMATIC EFFECTS

In this section, we briefly discuss some systematic effects that might have limited our analysis, such as the contamination from the background (instrumental and/or astrophysical) as well as the
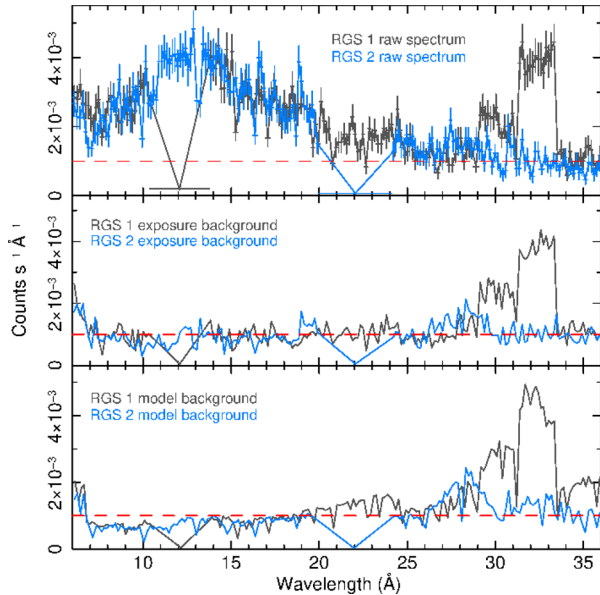
Figure A1. NGC 55 ULX *XMM* RGS 1–2 source raw spectra (top) with two alternative background spectra: exposure-extracted background (middle) and blank-field-model background spectra (bottom). The background is severe below ∼7 Å and above ∼26 Å and higher for RGS 1. RGS 1 and RGS 2 miss two chips covering the 10.4–13.8 Å and 20–24 Å range, respectively.

approximation of the ionization balance. We also provide some more technical detail on the selection of flux intervals used to extract flux-resolved spectra and the plots of the power density spectra. All this was shifted here to speed up the paper reading.

A1 RGS background

ULXs are faint sources if compared to common nearby Galactic X-ray binaries or active galactic nuclei. The EPIC-pn camera has a very large effective area, which provides a lot of counts and an energy band broad enough to constrain the spectral continuum of ULXs. RGS spectrometers distribute the photons in much more energy bins and therefore are much less sensitive. Searching for weak features in their spectra must therefore be a careful process, particularly when accounting for the background. Luckily, we have two ways of extracting an RGS background spectrum. The first method uses the photons outside a certain cross-dispersion slit, which according to the standard *XMM–Newton*/SAS routine is the 98 per cent of the PSF (see Fig. A1, middle panel). Another method uses a model background estimated with ultradeep exposures of blank fields and scaled by the count rate in the RGS CCD 9 where hardly any emission from the source is expected (see Fig. A1, bottom panel). The two background spectra are very similar and significantly dominate below ∼7 Å and above ∼26 Å. The RGS 1 and 2 raw source spectra (and the spectral features) are significantly stronger than the background in our wavelength range. For the work presented in this paper, we have used the background determined from the exposure, but we have repeated all the work using the model background and found no significant change in our results. All this shows that the background has minor systematic effects in our analysis.

A2 SED and ionization balance

Another source of systematic uncertainties is the choice of the spectral energy distribution (SED) since it may affect the ionization balance and therefore the calculation of ionization parameters and

Table A1. Systematic effects on the ionization balance. RGS fits improvements and details with of two alternative photoionized absorbers that use a default (*xabs*) and a measured (*pion*) ionization balance. The column densities are in standard units of 10^{24} cm^{-2}. The photoionization parameters are in log (ξ, erg cm s^{-1}). Outflow velocities are in units of light speed c.

Parameter	*xabs* model	*pion* model
N_{H}	$0.10^{+0.18}_{-0.03}$	$0.21^{+0.43}_{-0.12}$
$\log \xi$	3.35 ± 0.20	3.44 ± 0.29
v_{outflow}	0.199 ± 0.003	0.198 ± 0.003
$\Delta \chi^2/\Delta C$/dof	19/18/3	19/18/3

column densities in the photoionization components (both in emission and absorption).

For instance, the standard *xabs* model in SPEX adopts a Seyfert 1 type of SED and ionization balance, whose shape of course deviates from the soft SED of a ULX such as NGC 55 ULX. To understand the effects of the SED choice, we test the photoionization *pion* model in SPEX, which assumes the SED measured with the fitted spectral continuum model – the observed spectral shape of NGC 55 ULX – and instantaneously calculates the photoionization equilibrium using the plasma routines available in SPEX (see the SPEX manual for more detail). At the moment, the *pion* emission model calculates the thermal emission of the photoionized layer by ignoring the photon-induced processes. This is not realistic enough, so for the moment we only check the effects of the SED on the absorption component.

We have fitted again the RGS spectrum of NGC 55 ULX with the EPIC spectral continuum on the top of which we have added a *pion* model to substitute the *xabs* component of the 0.2*c* absorber detected with highest significance. The main result is shown in Table A1 along with the improvement in the fits previously obtained with the *xabs* model (see also Table 4). The results with the *xabs* and the *pion* models are consistent within the statistical uncertainties mainly due to the limited statistics. However, there is no indication of major systematics apart from the fact that the *pion* model has larger uncertainties due to the larger dependence of the parameters on the continuum shape. The *pion* model certainly provides a more physical description of the absorber(s), but it requires much more memory and CPU time than the *xabs* model, of course. The search for a multiple/continuous photoionization structure of the wind would have been prohibitive with as many *pion* components as the *xabs* components used in Section 4.2.5 and Fig. 7.

A3 EPIC light curves for flux-resolved spectra

In Section 4.3, we extracted EPIC spectra in different flux ranges in order to understand the dependence of its spectral shape with the luminosity. Here, we briefly describe the selection of the flux intervals.

At first, we extracted an EPIC/pn light curve in the 0.3–10 keV energy band for both the first (ID = 0028740201) and the second exposure (ID = 0655050101). The source and background regions were the same as those used to extract the spectra (see Section 3). The background light curves were subtracted with the *epiclccorr* task. The background-subtracted light curves are shown in Fig. A2.

We then split the two observation into five slices with comparable statistics. In the first observation, we selected bins with count rates above (or below) 1.895 count s^{-1}. This provided two slices with 27 000 counts each. The second observation was instead split
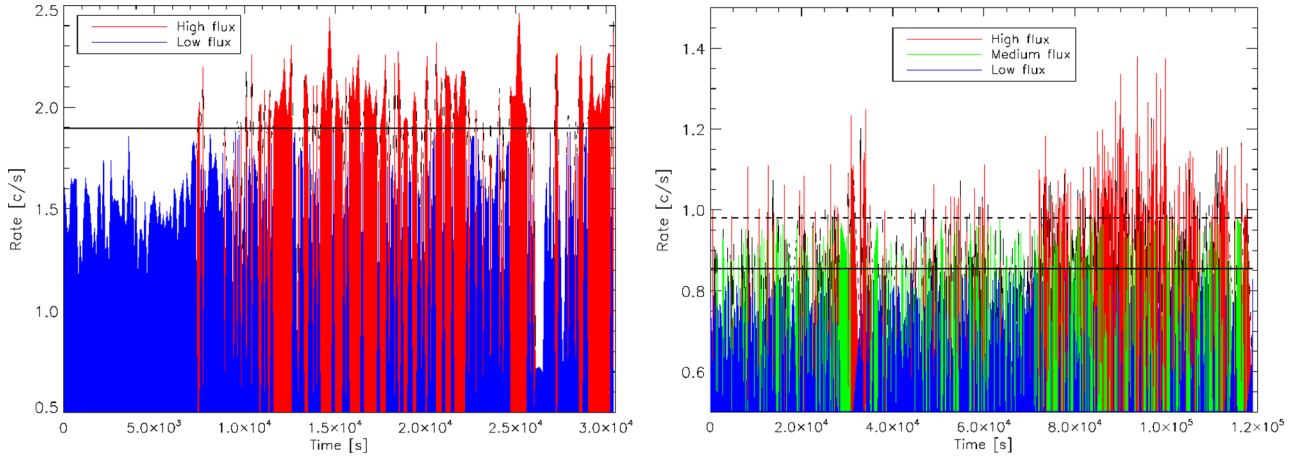
Figure A2. EPIC/pn 0.3–10 keV light curves of the first (left) and second (right) observations both with time bins of 100 s. Flux thresholds were chosen in order have comparable statistics. For more detail see the text.
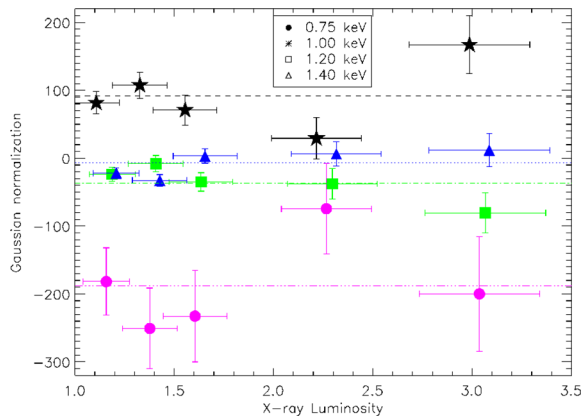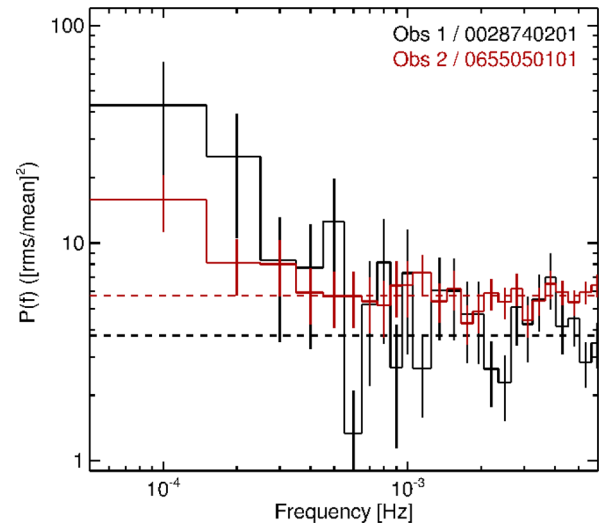

Figure A3. Gaussian fits to the flux-resolved EPIC pn spectra. Normalizations are in units of 10^{44} photons s^{-1}. Negative values refer to absorption lines. Luminosities are same as in Table 5. We slightly shifted the points along the *X*-axis for plotting purposes.

Figure A4. Power density spectra for the first (black) and second (red) observations computed in the 0.3–1.0 keV energy range. The dashed lines show the Poisson noise level.
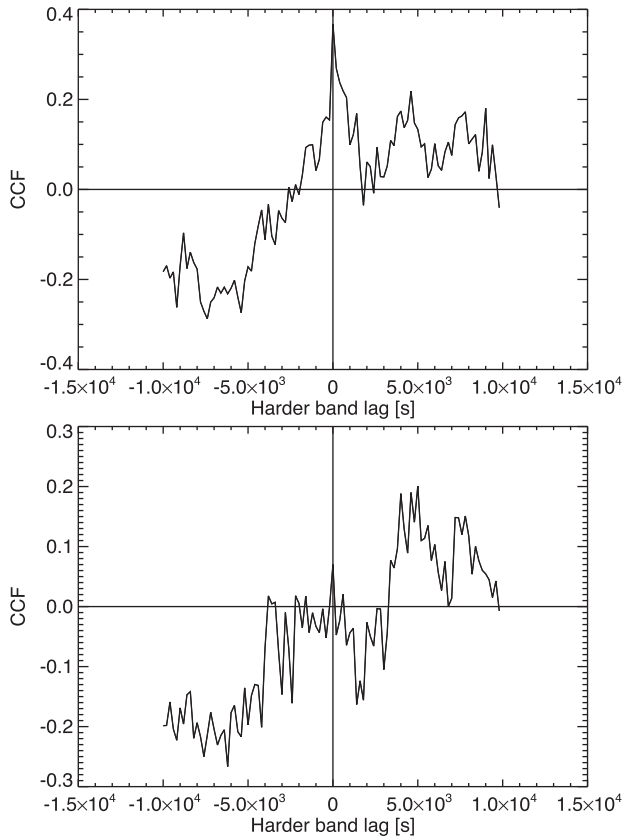
A5 Power density spectra

We follow the standard method of computing a periodogram in 10 ks light-curve segments before averaging over the segments at each frequency bin, and subsequent binning up over adjacent frequency bins (van der Klis 1989, Vaughan et al. 2003). The resulting power density spectra are shown in Fig. A4. Taking into account the level of Poisson noise, given by the dashed lines, it shows that the source has very limited variability in 2010 compared to 2001.

A6 Cross-correlation spectra

For completeness, we have also computed the cross-correlation (CCF) between the soft energy band (0.3–1.0 keV – same as reference band used in cross-spectrum, CS, throughout the paper) and several other bands. In Fig. A5, we show the CCF computed with respect to the 1.0–2.0 keV (top) and the 3.5–6.0 keV (bottom) energy bands. The harder band is always defined as having the positive lag on the *x*-axis.

The plot shows that there is clearly some lag structure in agreement with what we see in the CS. For the soft band separations,

into three intervals of fluxes between (<0.855), (0.855–0.980) and (>0.98) counts s^{-1}. This provided three slices with about 32 000 counts each. The statistics of these five time intervals are comparable. The five time intervals can also be seen in Fig. A2. We built the good time intervals using these intervals and extracted source and background spectra, response matrices and effective area auxiliary files with the *evselect* task. The flux-resolved spectra have been shown in Fig. 9.

A4 EPIC flux-resolved spectra: Gaussian fits

We tested the behaviour of the EPIC spectral residuals by fitting a Gaussian line for some of the strongest residuals (0.75, 1.0, 1.2 and 1.4 keV, see Fig. 3). We adopted a full width at half-maximum of 100 eV similar to the EPIC spectral resolution. We fit these four Gaussian lines with fix energies to the five flux-resolved spectra and show the results in Fig. A3. The lines are broadly consistent within their mean values, but there are a few deviations. Although there is hint for variability, we notice that deeper observations are needed to confirm and study their variability in detail.

Figure A5. CCF for the second observation computed between the (0.3–1.0 versus 1.0–2.0 keV, *top*) and the (0.3–1.0 versus 3.5–6.0 keV, *bottom*) energy bands. Notice the lag structure.

there is a strong correlation at zero time delay, with a skew towards a softer lag. As the energy band separation increases, the zero-lag correlation weakens, and we start to see a hard lag, as well as a negative lag. The changes seem to occur when looking at bands above ~ 0.9–1.0 keV, similar to where we see the changes in the covariance. The CCFs are however harder to interpret because they average over all the frequency dependent behaviour.

**Table A2.** *XMM–Newton* observations of non-ULX sources.

Source	Type	ID	$t^{(a)}_{RGS1}$ (ks)	$t^{(b)}_{RGS1}$ (ks)
PKS 521-365	BL Lac	0065760201	31.9	31.0
4U 241+61	Seyfert 1	0503690101	118.4	46.2
BL Lac	BL Lac	0504370401	133.9	83.5
PKS 537-441	BL Lac	0551503301	24.5	18.7
3C 279	Quasar	0651610101	126.3	107.7

[a]RGS nominal; [b]Net exposure time after BKG screening.

A7 RGS spectra of other sources

In order to confirm that the lines detected in NGC 55 ULX are not produced by instrumental features, we have searched for similar features in five extragalactic sources whose spectra are expected to be mainly featureless. We chose these objects because the statistics quality of their RGS spectra is comparable to the RGS spectrum of NGC 55 ULX, once accounted for the net exposure time and the flux. In Table A2, we report the detail of the exposures used. We repeat the RGS data reduction as done in Section 3 and the line search as described in Section 4.2.2 for these five sources.

In Fig. A6 (top), we show the results obtained with the line-search routine on each object adopting a power-law continuum corrected by redshift and Galactic absorption. In order to smear out any intrinsic features and strengthen the instrumental ones, we have also simultaneously fitted the RGS spectra of the five objects, adopting the best-fitting power-law continuum for each of them, whilst fitting the grid of Gaussian lines coupled between the models of the five spectra. In Fig. A6 (bottom), we compare the results from the line search obtained combining the five sources (solid line) with that one obtained for NGC 55 ULX (dotted line). At first, we notice that no emission feature is significantly detected at or above 3σ, but more importantly the strongest features detected in NGC 55 ULX are absent in the other sources and in their combined analysis. This shows that the lines detected in the RGS spectrum of NGC 55 ULX are significant and intrinsic to the source.
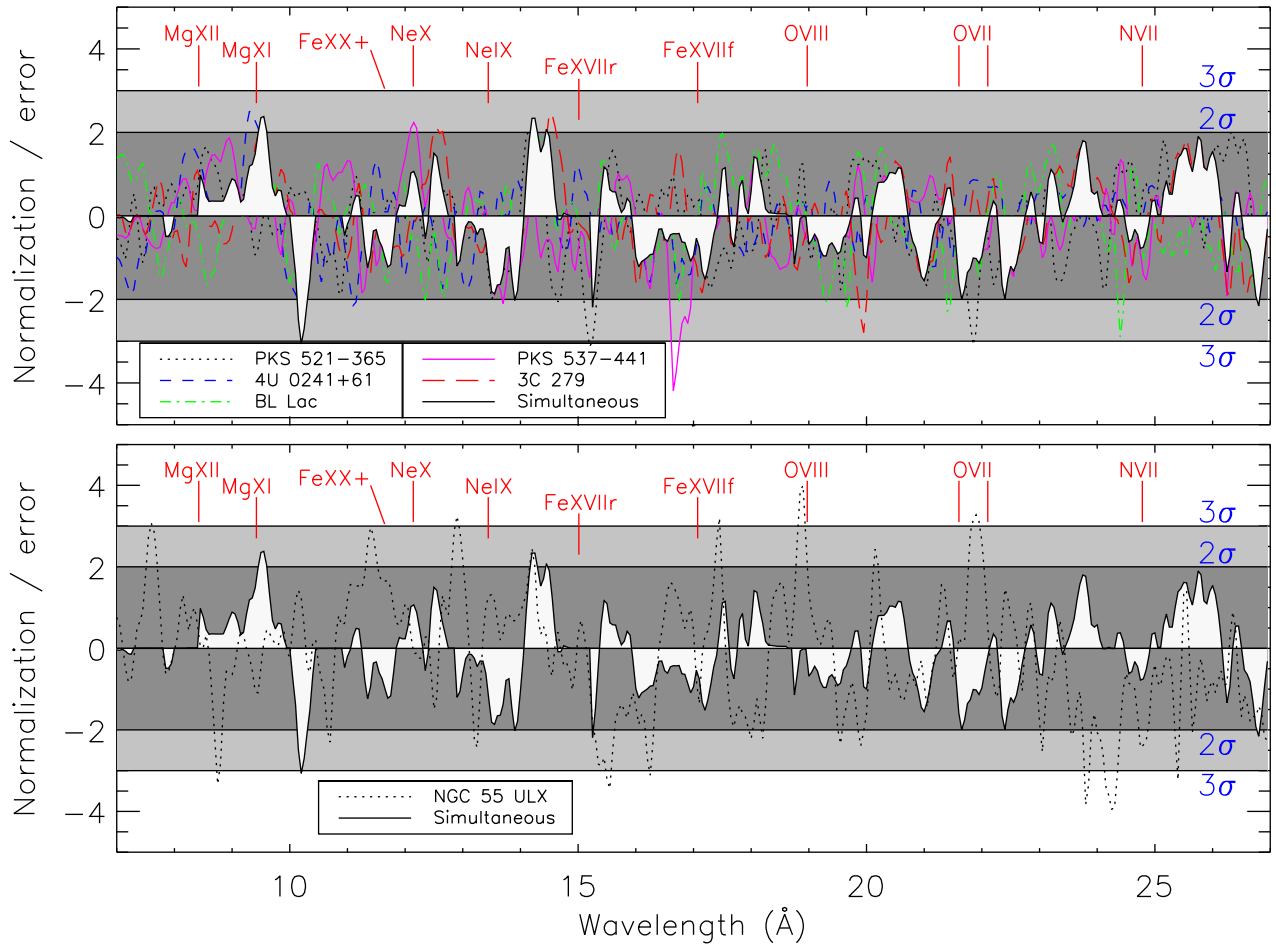
Figure A6. Line search for five power-law-like objects (top) and their simultaneous fits compared to that of NGC 55 ULX (bottom). The strong features detected in NGC 55 ULX significantly differ from the weak instrumental features present in the other objects.

This paper has been typeset from a TEX/LATEX file prepared by the author.